

Matrix viscoelasticity controls spatiotemporal tissue organization

Received: 1 October 2020

Accepted: 7 October 2022

Published online: 01 December 2022

 Check for updates

Alberto Elosegui-Artola^{1,2,3,4,5,12}, Anupam Gupta^{1,6,12}, Alexander J. Najibi^{1,2}, Bo Ri Seo^{1,2}, Ryan Garry¹, Christina M. Tringides^{1,2,7,8}, Irene de Lázaro^{1,2}, Max Darnell^{1,2}, Wei Gu⁹, Qiao Zhou⁹, David A. Weitz^{1,10}, L. Mahadevan^{1,10,11}✉ & David J. Mooney^{1,2}✉

Biomolecular and physical cues of the extracellular matrix environment regulate collective cell dynamics and tissue patterning. Nonetheless, how the viscoelastic properties of the matrix regulate collective cell spatial and temporal organization is not fully understood. Here we show that the passive viscoelastic properties of the matrix encapsulating a spheroidal tissue of breast epithelial cells guide tissue proliferation in space and in time. Matrix viscoelasticity prompts symmetry breaking of the spheroid, leading to the formation of invading finger-like protrusions, YAP nuclear translocation and epithelial-to-mesenchymal transition both in vitro and in vivo in a Arp2/3-complex-dependent manner. Computational modelling of these observations allows us to establish a phase diagram relating morphological stability with matrix viscoelasticity, tissue viscosity, cell motility and cell division rate, which is experimentally validated by biochemical assays and in vitro experiments with an intestinal organoid. Altogether, this work highlights the role of stress relaxation mechanisms in tissue growth dynamics, a fundamental process in morphogenesis and oncogenesis.

The patterning of tissues in space and time is relevant for many biological processes^{1–3}, and is driven by changes in cell number, size, shape and position that lead to symmetry-breaking instabilities such as buckling, folding, tearing, budding, fingering or branching^{4,5}. At a molecular level, the spatiotemporal organization of tissues is regulated by intrinsic gene expression⁶, and a variety of environmental chemical and mechanical cues⁷. While the importance of chemical morphogen gradients in development has long been appreciated⁸, it is increasingly clear that mechanical cues^{9–12} in the tissue and the surrounding three-dimensional (3D) extracellular matrix (ECM) also regulate tissue organization and morphogenesis. The role of stiffness in tissue organization has been

studied extensively^{1,13,14}. However, the role of viscosity versus elasticity of the matrix in the tissue response is unclear, although the time-varying viscoelastic properties of the ECM are increasingly thought to be an important player in morphogenesis^{15,16}. Indeed, matrix viscoelasticity has been shown to regulate single-cell behaviour¹⁵, but it is not known how it regulates collective behaviour. Thus, tissue organization is expected to be impacted by the viscoelastic properties of the matrix¹⁷ whose behaviours vary from an elastic solid-like response to a liquid-like viscous response, with stress relaxation time scales that range from a second to a few hundred seconds. Here we report an experimental and computational study of the role of the viscoelasticity of well-defined

¹Harvard John A. Paulson School of Engineering and Applied Sciences, Harvard University, Cambridge, MA, USA. ²Wyss Institute for Biologically Inspired Engineering, Cambridge, MA, USA. ³Institute for Bioengineering of Catalonia, Barcelona, Spain. ⁴Cell and Tissue Mechanobiology Laboratory, Francis Crick Institute, London, UK. ⁵Department of Physics, King's College London, London, UK. ⁶Department of Physics, Indian Institute of Technology Hyderabad, Hyderabad, India. ⁷Harvard Program in Biophysics, Harvard University, Cambridge, MA, USA. ⁸Harvard–MIT Division in Health Sciences and Technology, Massachusetts Institute of Technology, Cambridge, MA, USA. ⁹Weill Cornell Medicine, Cornell University, New York, NY, USA. ¹⁰Department of Physics, Harvard University, Cambridge, MA, USA. ¹¹Department of Organismic and Evolutionary Biology, Harvard University, Cambridge, MA, USA. ¹²These authors contributed equally: Alberto Elosegui-Artola, Anupam Gupta. ✉ e-mail: lmahadev@g.harvard.edu; mooneyd@seas.harvard.edu

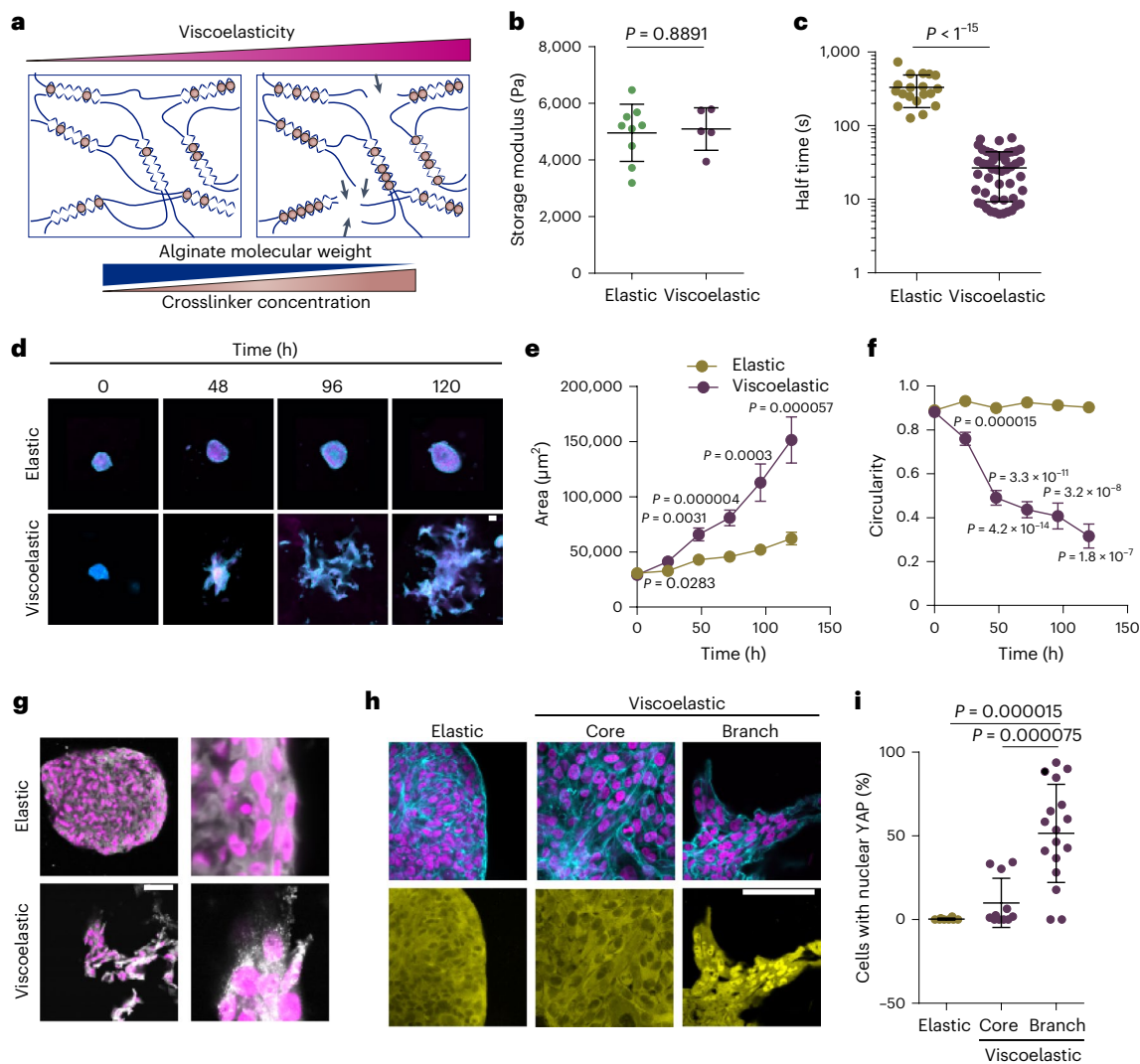


Fig. 1 | Matrix viscoelasticity determines symmetry breaking, tissue branching and EMT. **a**, Schematic demonstrating how simultaneously changing the polymer molecular weight and extent of crosslinking allows for constant gel stiffness but altered viscoelastic properties. **b**, Quantification of the storage modulus of resulting alginate hydrogels ($n = 5, 9$ gels per condition). **c**, Quantification of the time scale at which an initially applied stress is relaxed to half its original value ($n = 19$ gels per condition). **d**, Examples of growth of MCF10A spheroids in elastic versus viscoelastic hydrogels over 5 days. Cyan, phalloidin; magenta, Hoechst. **e, f**, Quantification of the spheroid area (**e**) and circularity (**f**). Error bars, s.e.m. $n = 19$ –43 spheroids per condition per day. **g**, Representative examples of phosphorylated FAK focal adhesions in MCF10A

cell spheroids growing in elastic and viscoelastic gels. Grey, pFAK; magenta, Hoechst ($n = 3, 4$ images per condition). **h**, Representative examples of phalloidin (cyan), Hoechst (magenta) (upper row) and YAP (lower row) stainings of spheroids in elastic and viscoelastic gels (spheroid core cells and branch leader cells). **i**, Quantification from stainings of the percentage of cells with nuclear YAP per image for the indicated regions ($n = 8, 11, 17$ images per condition). Statistical analysis was performed using the Kruskal–Wallis test followed by a post hoc Dunn’s test. For **b, c, e, f**, statistical analysis was performed using a two-sided Mann–Whitney U-test. All data are mean \pm s.d. except where indicated. Scale bars, 75 μm .

model matrices in regulating tissue organization in two commonly used *in vitro* models of development and pathology, breast epithelial growth¹⁸ and intestinal organoid development². These studies demonstrate the role of stress relaxation in determining the dynamics of tissue growth and the symmetry-breaking instabilities associated with fingering, a fundamental process in morphogenesis and oncogenesis.

Results

ECM viscoelasticity regulates epithelial tissue organization

We first studied the importance of matrix viscoelasticity in the organization and growth of mammary tissues from spheroids of MCF10A non-malignant breast epithelial cells. Hydrogels formed from the natural polysaccharide alginate were chosen as the model matrix system because mammalian cells do not express enzymes to degrade

these polymers, allowing effects related to matrix degradation to be eliminated¹⁹. The relative viscoelastic properties of these gels can be readily altered independently of the stiffness, pore size and adhesive ligands²⁰. This was achieved here by changing the molecular weight of alginate and the calcium crosslinker density in concert (Fig. 1a) to create gel matrices of constant elastic moduli ($G' \approx 5,000$ Pa) (Fig. 1b), but varying stress relaxation times ($\tau_m = 30$ –350 s) to achieve matrices that are more elastic ($\tau_m \approx 350$ s) or more viscoelastic ($\tau_m \approx 30$ s) (Fig. 1c). As alginate does not present intrinsic integrin adhesion ligands, Arg–Gly–Asp (RGD)-containing peptides were conjugated to the polymer backbone to provide a constant level of cell binding sites in all gels²¹. MCF10A breast epithelial cells, widely used to study mammary development and oncogenesis¹⁸, were formed into spheroids of $\sim 2,000$ cells and encapsulated in hydrogels.

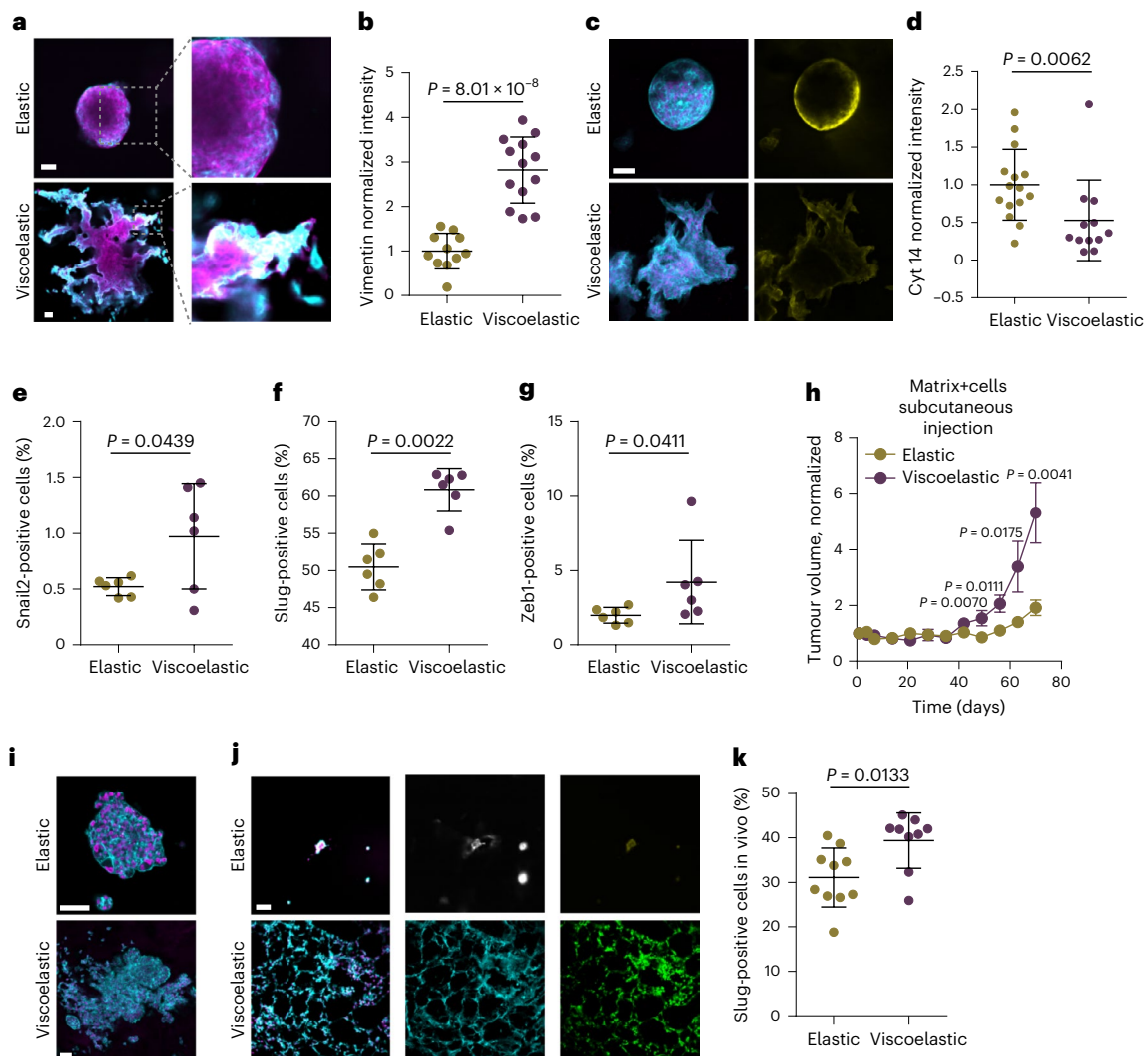
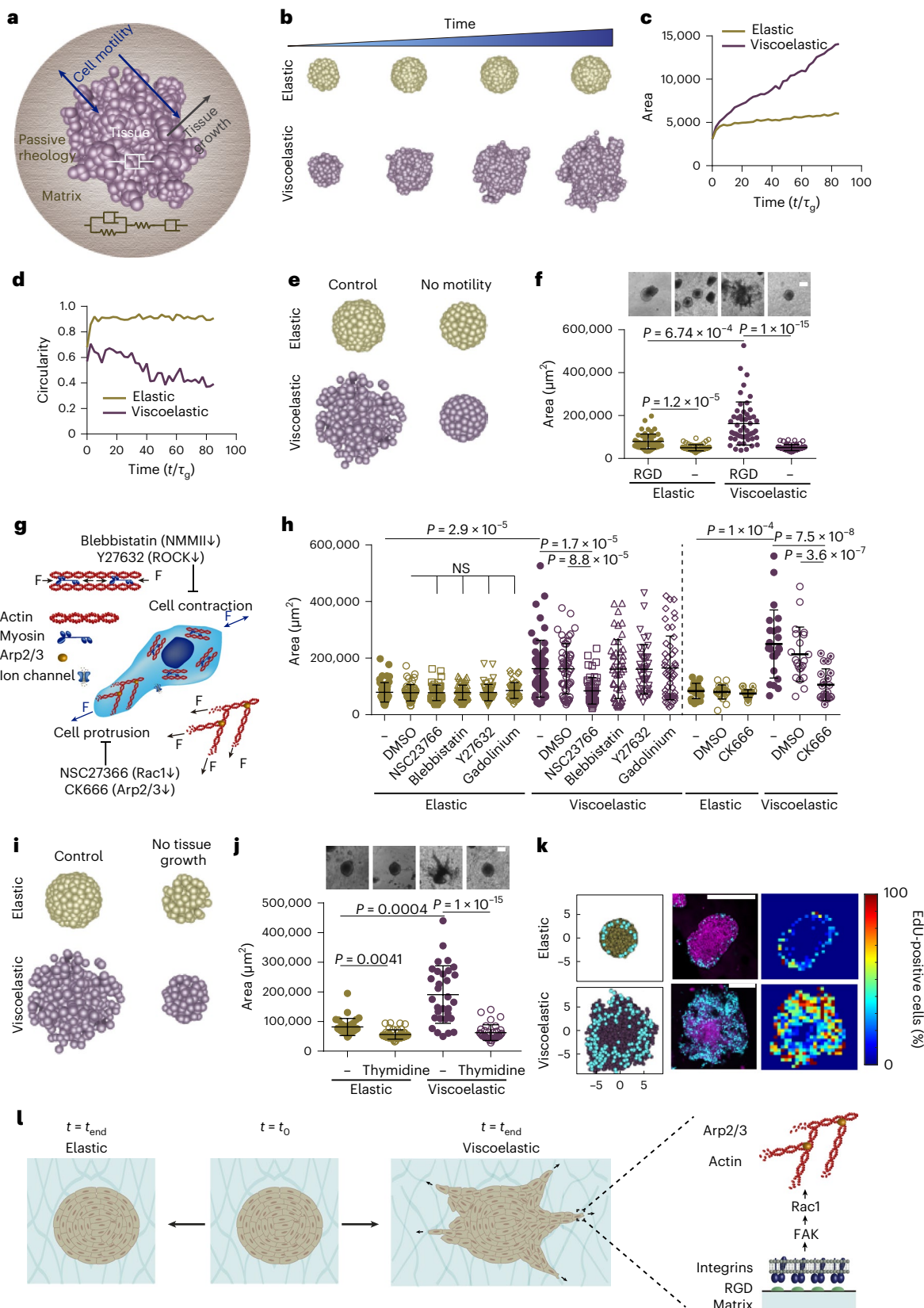


Fig. 2 Matrix viscoelasticity promotes EMT and tumour growth. **a**, Examples of vimentin (cyan), phalloidin (magenta) stainings in spheroids growing in viscoelastic gels. Insets shows the high expression of vimentin in the fingering instability arising from the spheroid. **b**, Quantification of average vimentin intensity in the outer ring of spheroids in elastic hydrogels and in fingers of spheroids in viscoelastic hydrogels. Average intensity of the elastic spheroid is normalized to 1. $n = 11$, 13 spheroids per condition. **c**, Examples of phalloidin and Hoechst (left) and cytokeratin 14 (right) stainings in spheroids in viscoelastic and elastic hydrogels. Cyan, phalloidin; magenta, Hoechst; yellow, cytokeratin 14. **d**, Quantification of average cytokeratin 14 intensity of the outer ring of spheroids. Elastic spheroid average intensity is normalized to 1. $n = 12$, 15 spheroids per condition. **e–g**, Quantification of percentage of Snail (**e**), Slug (**f**) or Zeb1 (**g**) positive cells in spheroids in elastic and viscoelastic matrices. $n = 6$, 6 gels

per condition. **h**, Quantification of the tumour volume in mice injected on day 0 with viscoelastic and elastic hydrogels containing MDA-MB-231 breast epithelial cells. Error bars, s.e.m. $n = 7$ mice per condition. **i**, Representative examples of phalloidin and Hoechst stainings of MDA-MB-231 in elastic and viscoelastic hydrogels. $n = 8$, 7 images per condition. Cyan, phalloidin; magenta, Hoechst. **j**, Representative examples of phalloidin and Hoechst (left), mitochondria (centre) and vimentin (right) stainings of MCF10A spheroids in viscoelastic and elastic hydrogels implanted in nude mice, 7 days after implantation. $n = 5$, 7 images per condition. **k**, Quantification of percentage of Slug-positive cells in spheroids in elastic and viscoelastic matrices implanted in mice, 7 days after implantation. $n = 10$ gels per condition. Statistical analysis was performed using a two-sided Mann–Whitney *U*-test. All data are mean \pm s.d. except where indicated. Scale bars, 75 μ m.

Over time, tissues in elastic matrices grew slowly and were morphologically stable; they increased in size while maintaining their spherical symmetry. However, tissues in viscoelastic matrices grew much faster. As they increased in size, they exhibited morphological instability and broke spherical symmetry, formed fingers and invaded the matrix, leading to a significant increase in the surface area and a decrease in circularity (Fig. 1d–f, Extended Data Fig. 1a and Supplementary Video 1). As these differences resulted from changes in the mechanical properties of the matrix, our studies next focused on two major mechanosensitive hubs in cells, the focal adhesion kinase (FAK) complex, and the mechanosensitive transcriptional regulator yes-associated protein (YAP)²². Viscoelastic matrices promoted the

expression and formation of phosphorylated pFAK adhesions, but elastic matrices did not (Fig. 1g and Extended Data Fig. 1d,e), while YAP remained in the cytoplasm in cells in elastic matrices, but translocated to the nucleus in cells in fingers in viscoelastic matrices (Fig. 1h,i). Although YAP nuclear translocation has been observed at the single-cell level in 3D viscoelastic matrices²⁰, it has also been observed that YAP was not mechanosensitive in 3D spheroids of MCF10A cells²³. However, we used more rapidly relaxing matrices than used in that earlier study²³, supporting a viscoelasticity-sensitive mechanism. When FAK was inhibited (Extended Data Fig. 1b,c), breast epithelium was morphologically stable, confirming the importance of mechanotransduction. Despite differences in YAP localization, no significant differences in nesprin or



emerin expression were observed in spheroids in elastic or viscoelastic matrices (Extended Data Fig. 1f,g). When proliferation was inhibited with thymidine, YAP was mainly cytoplasmic in viscoelastic matrices (Extended Data Fig. 1h).

The behaviour observed in viscoelastic matrices is seen in many biological processes that demonstrate symmetry-breaking

accompanied by epithelial-to-mesenchymal transitions (EMTs)²⁴. In agreement with that precedent, cells in viscoelastic matrices demonstrated an EMT, as vimentin was expressed in fingers (Fig. 2a,b), cytokeratin 14 expression was low in cells in spheroids in viscoelastic matrices (Fig. 2c,d) and the EMT transcription factors Snail, Slug and Zeb1 were more expressed in cells in viscoelastic matrices (Fig. 2e-g,

Fig. 3 | Theoretical model predicts that spheroid–material physical interaction regulates tissue geometrical evolution. **a**, Schematic depicting theoretical physical model of tissue growth in a passive viscoelastic matrix. The viscosity of the tissue, the viscosity of the matrix and the elasticity of the matrix can be tuned independently. **b**, Examples of simulated tissue growth in elastic matrices (top row) versus viscoelastic matrices (lower row). **c,d**, Quantification from simulations of the projected area (**c**) and circularity (**d**) of the spheroids over normalized time. τ_g , the constant time scale to add one cell to the tissue in the absence to stress. **e**, Model prediction with inhibition of cell motility. **f**, Representative experimental examples (upper row) and quantification of spheroid area (lower row) in hydrogels after 5 days in gels with and without cell adhesive ligand RGD. $n = 52, 52, 51, 54$ spheroids per condition. **g**, Schematic showing inhibitors used to affect cell motility: (1) Blebbistatin and Y27632 affect the actomyosin cytoskeleton by affecting non-muscle myosin II (NMMII) and ROCK, respectively; (2) cell protrusion is affected by NSC23766 and CK666 that affect Rac1 and the Arp2/3 complex, respectively; and (3) gadolinium affects ion channels. F, force. **h**, Quantification of the spheroid area after 5 days in the presence of the indicated inhibitors. $n = 52, 50, 51, 51, 51, 50, 51, 50, 51, 46, 41,$

51, 21, 21, 24, 20, 21, 25 spheroids per condition. NS, not significant. **i**, Model predictions with tissue growth inhibition. **j**, Representative experimental examples and quantification of spheroid's area without or with thymidine to inhibit cell proliferation. $n = 52, 53, 51, 53$ spheroids per condition. **k**, Model predictions and experimental results for the numbers and distributions of proliferating cells across spheroids in elastic (upper row) and viscoelastic gels (lower row); left, model predictions of localization of cell division (cyan) from a section of a spheroid; centre, representative examples of experimental spheroids showing EdU-positive cells (cyan) and cell nuclei (Hoechst, magenta) for spheroids in elastic and viscoelastic gels; right, colourmaps of experimental image (centre) showing the local percentage of EdU-positive cells across the spheroid. $n = 3, 4$ spheroids per condition. **l**, Altogether, data indicate that the ability of growing tissues to break symmetry and exhibit fingering in viscoelastic matrices is dependent on integrin adhesion, FAK phosphorylation, Rac1 activity and Arp2/3. Inhibiting these elements prevents tissue morphological instability. Statistical analysis was performed using a Kruskal–Wallis test followed by a post hoc Dunn's test. All data are mean \pm s.d. Scale bars, 200 μ m.

Supplementary Fig. 1 and Extended Data Fig. 2). Furthermore, a number of cancer-related pathways were not altered in cells within elastic matrices, but were upregulated in viscoelastic stiff hydrogels (Supplementary Fig. 2). To determine whether viscoelasticity enhanced tissue growth in vivo we followed two approaches. First, MDA-MB-231 malignant breast epithelial cells encapsulated either in viscoelastic or elastic matrices were injected in NOD-SCID mice. Tumours grew significantly more rapidly in viscoelastic than in elastic matrices (Fig. 2h and Supplementary Fig. 3). MDA-MB-231 cells also grew more rapidly in vitro (Fig. 2i and Extended Data Fig. 2h,i). Second, MCF10A spheroids encapsulated either in viscoelastic or elastic matrices were injected in NU/J mice. After 1 week, we observed significant growth and fingering in cells in viscoelastic matrices, while the cells in elastic matrices showed only limited growth (Fig. 2j). Additionally, these cells in vivo expressed significantly more vimentin (Fig. 2j) and Slug (Fig. 2k and Extended Data Fig. 2f,g) in viscoelastic matrices. While previous studies have shown that spheroids in elastic matrices are unable to break symmetry and invade^{25,26}, our results demonstrate that matrix viscoelasticity can promote EMT and tumour growth.

Our experiments show that more elastic matrices ($\tau_m \approx 350$ s) resist tissue invasion, whereas viscoelastic matrices ($\tau_m \approx 30$ s) are easily invaded by the motile and proliferating cells. Similarly, our observations show that tissues which are highly proliferative lead to an increase in cell influx and probably generate a mechanical pressure that drives the morphological instability of the tissue–matrix interface. These observations of fingering morphologies in active biological systems have physical analogues that have been studied for decades in simple and complex fluids^{27,28}. Our experimental observations suggest that the combination of biological activity due to cell migration and/or

proliferative pressure at the tissue–matrix interface may lead to a similar symmetry-breaking instability exemplified by fingering or branching.

Computational model recapitulates tissue organization

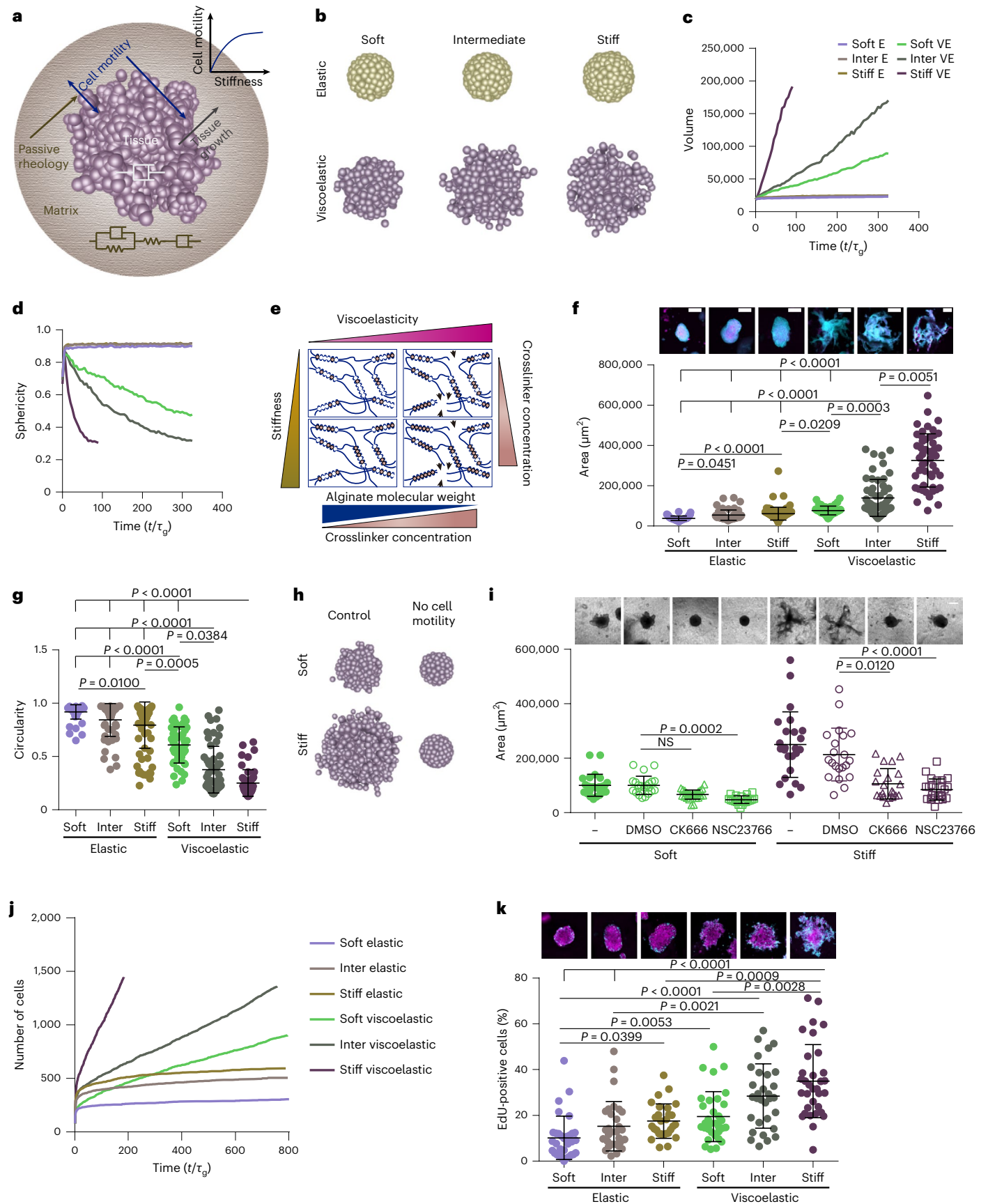
To understand how the conditions for tissue morphological instability emerge, we consider a minimal theoretical model of the system (Fig. 3a and Extended Data Fig. 3) starting from a two-phase system of active proliferating cells growing inside a confining passive viscoelastic matrix. We model the individual cells in the tissue as overdamped soft elastic spheres of size a in a liquid of effective viscosity μ_c , which move under the influence of three forces: (1) the interaction between cells, with (a) a short-range repulsion to prevent overlap and (b) a mid-range (two cell-length) attraction with the depth in the attractive well ε (see Supplementary Information for details) which together lead to an active proliferative pressure driven by cell division; (2) the repulsion between the cell and the surrounding viscoelastic matrix (modelled as a set of similar spheres of size a in a liquid of effective viscosity μ_m interacting with each other via (a) an attractive potential—equivalent to storage modulus G' —and (b) a short-range repulsion to prevent overlap); and (3) the activity of cells that are assumed to move randomly relative to each other in the bulk, characterized by a motility parameter M (or an effective temperature)²⁹. Additionally, in the model, the cells at the interface are assumed to have the ability to apply forces to the surrounding matrix³⁰. The system evolves as cells proliferate and/or migrate actively and the matrix responds passively to the accompanying forces. In particular, the bonds between the spheres in the matrix as well as those between the cells and the matrix can break when strained beyond a prescribed threshold, allowing new bonds to

Fig. 4 | Stiffness intersects with matrix viscoelasticity to regulate growth and branching. **a**, To incorporate the matrix stiffness dependence on the tissue property, the active motility of the tissue is now an increasing function of the matrix stiffness, which makes the active motility a dependent parameter and in turn also affects the tissue growth. **b–d**, 3D final time point simulation images (**b**), projected area (**c**) and circularity (**d**) evolution over normalized time of spheroids in increasingly stiff elastic (E) and viscoelastic (VE) gels. **e**, Stiffness of experimental matrices was modified by further altering the extent of crosslinking in both elastic and viscoelastic gels. **f**, Representative experimental examples (upper row) and quantification of spheroid area (lower row) after 5 days in elastic and viscoelastic matrices of increasing stiffness. $n = 63, 55, 84, 50, 55, 50$ spheroids per condition. Statistical analysis was performed using a Kruskal–Wallis test followed by a post hoc Dunn's test. **g**, Quantification of spheroid circularity after 5 days in elastic and viscoelastic matrices of increasing stiffness. $n = 63, 55, 84, 50, 55, 50$ spheroids per condition. Statistical analysis was performed using a

Kruskal–Wallis test followed by a post hoc Dunn's test. **h**, Representative model simulation results when cell motility is eliminated in stiff viscoelastic matrices compared to soft viscoelastic matrices. **i**, Representative experimental examples (upper row) and quantification of spheroid area (lower row) after 5 days in soft and stiff viscoelastic matrices with Rac1 (NSC23766) and Arp2/3 (CK666) inhibitors. $n = 25, 22, 27, 21, 24, 21, 21, 24$ spheroids per condition. Statistical analysis was performed using a Kruskal–Wallis test followed by a post hoc Dunn's test. **j**, Model predictions for cell proliferation in spheroids of increasing stiffness for both elastic and viscoelastic gels. **k**, Representative experimental examples (upper row) and quantification of the percentage of EdU-positive cells in a spheroid (lower row) after 5 days in elastic and viscoelastic gels of increasing stiffness. $n = 32, 30, 28, 33, 31, 33$ spheroids per condition. Statistical analysis was performed using a Kruskal–Wallis test followed by a post hoc Dunn's test. τ_g , the constant time scale to add one cell to the tissue in the absence to stress. All data are mean \pm s.d. Scale bars, 200 μ m.

form; this is most likely to happen at the interface between the tissue and the matrix, and allows the boundary between the two phases to evolve dynamically.

The parameters in the model allow us to define three dimensionless variables to characterize the scaled matrix fluidity, the passive mechanical relaxation time of the matrix and the relative proliferative



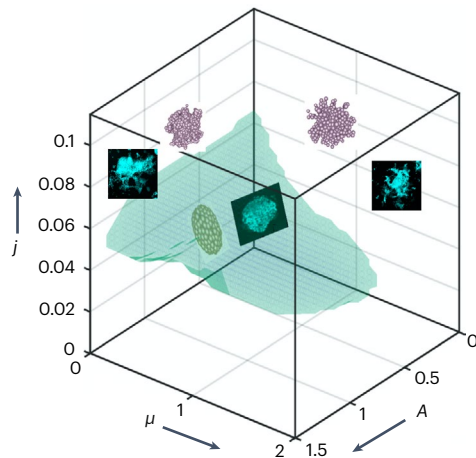


Fig. 5 | Springer Nature or its licensor (e.g. a society or other partner) holds exclusive rights to this article under a publishing agreement with the author(s) or other rightsholder(s); author self-archiving of the accepted manuscript version of this article is solely governed by the terms of such publishing agreement and applicable law. Phase diagram. Simulations predict, and experiments confirm, that regions of tissue growth stability and instability can be predicted based on the values of three dimensionless variables. When the scaled proliferation pressure $j = \frac{\tau_g}{\tau_t} \ll 1$, the tissue grows as a stable spheroid (Fig. 3i,j, Extended Data Fig. 8b, and Supplementary Figs. 8 and 9). Additionally, when the scaled matrix relaxation time $A = \frac{\tau_a}{\tau_m} \ll 1$, the tissue remains spheroidal and is morphologically stable as long as the scaled proliferation pressure $j = \frac{\tau_g}{\tau_t} \approx O(1)$ (top panel of Figs. 1d, 3b and 4b). When the scaled matrix relaxation time $A = \frac{\tau_a}{\tau_m} \gg 1$: if the scaled proliferation pressure $j = \frac{\tau_g}{\tau_t} \ll 1$, the tissue grows as a stable spheroid (bottom right of Fig. 3i and bottom panel of Supplementary Fig. 8b); if the scaled proliferation pressure $j = \frac{\tau_g}{\tau_t} \approx O(1)$, the growth is unstable and the tissue breaks symmetry and develops branches (bottom panel of Figs. 1d, 3b and 4b); if the scaled proliferation pressure $j = \frac{\tau_g}{\tau_t} \gg 1$, the morphological stability of the tissue depends on $\mu = \frac{\mu_t}{\mu_m}$ (Extended Data Figs. 7d,e and 8c); for $\mu = \frac{\mu_t}{\mu_m} \ll 1$, the tissue remains spheroidal (Extended Data Figs. 7d,e and 8c); for $\mu = \frac{\mu_t}{\mu_m} \gg 1$, growth is unstable and the tissue breaks symmetry and develops branches (Extended Data Figs. 7d,e and 8c). Shown here are representative images from the experiments and the simulations in different regimes of the phase diagram; one set of images from stable tissues in the red region ($A = \frac{\tau_a}{\tau_m} = 0.4$; $\mu = \frac{\mu_t}{\mu_m} = 0.002$, $j = \frac{\tau_g}{\tau_t} = 0.05$) top left is the first set of unstable images from a specific point ($A = \frac{\tau_a}{\tau_m} = 400$; $\mu = \frac{\mu_t}{\mu_m} = 2$, $j = \frac{\tau_g}{\tau_t} = 0.22$) and top right is a second set of images of another unstable point ($A = \frac{\tau_a}{\tau_m} = 3.3$, $\mu = \frac{\mu_t}{\mu_m} = 2$, $j = \frac{\tau_g}{\tau_t} = 0.14$).

capacity of the tissue: (1) $\mu = \frac{\mu_t}{\mu_m}$, the ratio of the tissue viscosity μ_t to the matrix viscosity μ_m ; (2) the cell flux $j = \frac{\tau_g}{\tau_t}$, the ratio of the constant time scale to add one cell to the tissue in the absence to stress, τ_g , and the time scale to add one cell to the confined tissue in the presence of stress, τ_t ; and (iii) $A = \frac{\tau_a}{\tau_m}$, the ratio of the cell activity time scale $\tau_a = \frac{\tau_g}{\epsilon} M$, where M is the effective motility and ϵ is the strength of cell–cell adhesion, and the matrix relaxation time scale, $\tau_m = \frac{\mu_m}{G'}$, where G' is the shear (storage) modulus of the matrix. Each of these dimensionless parameters can be large or small (relative to unity) and play a role in controlling the morphological stability of the growing tissue (Supplementary Note 1).

We start our simulations within this framework with a spherical ball of cells that is loosely packed within a viscoelastic matrix, and then allow the cells to divide and push each other into the matrix, straining it. Depending on the rheology of the matrix, cell division can either (1) cause the matrix to break, flow and be remodelled even as tissue cells

form finger-like protrusions; or (2) cause the matrix to respond purely elastically by straining, but not breaking, thus preventing the cells from further division and maintaining a spherical boundary with the matrix. Indeed, as we decrease the relaxation time scale making the matrix behave more like a liquid (that is, making $A = \frac{G'}{\mu_m} \tau_a$ large by decreasing μ_m), we see the appearance of an interfacial morphological instability (Fig. 3b–d, Extended Data Fig. 3b,c, Supplementary Fig. 4, and Supplementary Videos 2, 4 and 5), in accordance with findings of experiments (Fig. 1). Additionally, when cell motility was reduced (by changing M), the model predicts that tissues growing in matrices would be unable to grow, break symmetry or form fingers (Fig. 3e and Extended Data Fig. 4a,b).

To test these predictions, we first carried out experiments using matrices without cell adhesion ligands, as cell adhesion and thus motility would be lost in this condition ($A = \frac{G'}{\mu_m} \tau_a \approx 0$). Tissues were found to grow slowly, in a morphologically stable manner (Fig. 3f, Extended Data Fig. 4c and Supplementary Video 3). Next, potential mechanisms driving tissue motility and proliferation at the cellular scale were explored. Contrary to previous studies where the response of single cells to 3D and 2D viscoelasticity was regulated by actomyosin contractility or stretch ion channels^{31,32}, only the inhibition of Rac1 or the Rac1 pathway downstream molecule Arp2/3 by pharmacological inhibitors (NSC23766 and CK666, respectively) inhibited tissue growth (Fig. 3h and Extended Data Fig. 4d,e), in accordance with our model predictions. Notably, formin inhibition did not affect the tissue response to viscoelasticity (Extended Data Fig. 4f,g). Our results show that the Arp2/3 complex regulates collective cell response only in viscoelastic matrices, as no effect of CK666 was found in elastic matrices (Fig. 3h and Extended Data Fig. 4d,e). This finding indicates that cells generate space for division and migration by pushing on the matrix. Consistent with this, when the rate of cell proliferation in the model was inhibited ($j = \frac{\tau_g}{\tau_t} \approx 0$), simulations predicted tissue growth and instability would be dramatically diminished (Fig. 3i, Extended Data Fig. 5a,b and Supplementary Video 6). Experiments confirmed this prediction (Fig. 3j and Extended Data Fig. 5c). Further, the model predicts that for cells in an elastic matrix, cell division would be spatially confined to the boundary between the growing tissue and the substrate, but for cells in a viscoelastic matrix, the divisions would be more broadly distributed throughout growing tissues (Fig. 3k and Extended Data Fig. 6). Experimental analysis of the spatial distribution of proliferating cells confirmed these predictions as well (Fig. 3k and Extended Data Fig. 6). Altogether, these results highlight the role of cellular adhesion, FAK, Rac1 and Arp2/3 in allowing for tissue morphological instability in viscoelastic matrices (Fig. 3l).

Having considered the role of matrix viscoelasticity and cell proliferation on tissue organization, we now turn to adapt our computational model to include the experimentally known role that links an increase in matrix stiffness with an increase in cell motility³³. We assume a minimal model, via the relation $M \propto G'$ (Fig. 4a). Simulations with this assumption predicted that tissue morphological instability would be enhanced with an increase in the modulus of the matrix G' in viscoelastic matrices (making $A = \frac{G'}{\mu_m} \tau_a$ large), but no significant impact in more elastic matrices (Fig. 4b–d, Supplementary Fig. 4, Supplementary Fig. 5 and Supplementary Video 5). To validate these simulations experimentally, the previously developed matrices were modified to change their modulus G' and independently control the relaxation time (by changing the molecular weight of alginate) to make the matrix more or less viscoelastic (Fig. 4e, Supplementary Figs. 6 and 7a, and Supplementary Table 1). In low viscosity matrices, that is, large $A = \frac{G'}{\mu_m} \tau_a$, the increase in the modulus G' resulted in greater tissue growth and fingering, as predicted (Fig. 4f,g and Extended Data Fig. 6b,c). Taking into account these results, we can rationalize previous apparently contradictory findings that tissues maintained a stable morphology

when encapsulated in synthetic materials²⁵ of increasing stiffness, while becoming unstable in natural matrices as the stiffness was raised⁴ (for example, Matrigel, collagen, fibrin). From our perspective, the explanation is due to the elastic nature of the synthetics that are covalently crosslinked, in contrast to the intrinsic viscoelasticity of physically crosslinked natural matrices.

To further determine if these differential responses were again mediated by cell motility and proliferation, *in silico* predictions were compared to *in vitro* studies performed under similar conditions. As predicted by the model, inhibition of cell motility by inhibition of Rac1 and Arp2/3 complex led to a greater impact on tissue growth in stiff matrices, that is, large $A = \frac{G'}{\tau_a}$ rather than soft viscoelastic matrices, that is, small $A = \frac{G'}{\tau_a}$ (Fig. 4h,i, Supplementary Fig. 8 and Supplementary Video 6). Both simulations and experiments revealed that cell division increased with stiffness both in elastic and viscoelastic matrices although significantly more in viscoelastic matrices (Fig. 4j,k and Supplementary Fig. 4a). The significant increase in cell flux with modulus G' in the viscoelastic matrices ($A = \frac{G'}{\tau_a}$ is large) emerges from the increase in motility M (ref. 33). When cell proliferation is inhibited, the simulations show that tissues do not grow (Supplementary Fig. 9 and Supplementary Video 7).

Having studied the emergence of an active scaled cell flux from motility M (with $j = \frac{\tau_g}{\tau_a} \approx O(1)$), we turn to passively inject a cell flux to the tissue (making $j^t = \frac{\tau_g}{\tau_a} \gg 1$) to examine the role of passive tissue pressure, known to regulate tissue growth^{12,34}, on morphological stability. We developed a microfluidic system where cells were injected at a constant rate into the tissue, displacing the matrix (Extended Data Fig. 7). We find that tissues break symmetry and finger out into elastic matrices but are unable to break symmetry when the matrix is viscoelastic, consistent with our simulations that show a similar response (Extended Data Figs. 7 and 8c, Supplementary Fig. 10 and Supplementary Video 8). The morphological instability occurring in this cell-flux-driven situation is similar to the Saffman–Taylor instability²⁷. Altogether, our simulations and experiments show that the tissue–matrix interface becomes morphologically unstable when the matrix is viscoelastic and can easily relax in response to stresses, or when the tissue proliferative pressure is high in more elastic matrices (Supplementary Table 3). We summarize these results in a morphological phase diagram that quantifies the stability of the growing front shown in Fig. 5 and Extended Data Fig. 8.

ECM viscoelasticity drives intestinal organoid morphogenesis

To explore the generality of the findings in the phase diagram, we explored the impact of matrix viscoelasticity on the growth of self-organizing intestinal organoids. When Lgr5⁺ stem cells are placed in Matrigel, they develop into complex 3D structures that mimic intestinal tissue organization². To allow for a comparison with the published literature, we modified our alginate matrix system to enable incorporation of Matrigel (Fig. 6a and Extended Data Fig. 9 and Supplementary

Fig. 11), while still allowing independent control over gel stiffness and viscoelasticity³⁵. As shown previously³⁵, the alginate–Matrigel matrices formed homogeneous interpenetrating networks (Supplementary Fig. 11). Interpenetrating networks of three different stiffnesses ($G' \approx 0.5, 1.5, 2.7$ kPa) allowed for both elastic and viscoelastic matrices (Fig. 6b, Supplementary Fig. 12 and Supplementary Table 3). As previously described³⁶, organoids, composed of a few cells or single cells, growing in elastic matrices exhibited slow expansion and were morphologically stable. In contrast, intestinal organoids grew rapidly, broke symmetry and formed fingers when within viscoelastic matrices (Fig. 6c–e, Extended Data Fig. 9 and Supplementary Fig. 13). The slow organoid development found in elastic gels is consistent with past studies utilizing purely elastic polyethylene glycol materials³⁶. Organoid growth in the polyethylene glycol elastic materials required fast matrix degradation³⁶, which will alter a number of matrix features, including porosity and mechanical properties, while we demonstrate that matrix viscoelasticity regulates this process. Apart from demonstrating tissue morphological instability, intestinal organoids in viscoelastic substrates exhibited cell patterning and differentiation representative of intestinal development (Fig. 6f,g and Extended Data Fig. 10c–f). Matrix viscoelasticity favoured the generation of high-curvature tissue regions that concentrated Lgr5⁺ stem cells (Extended Data Fig. 10a,b), consistent with past reports on the impact of curvature¹¹. No significant differences in organoid morphology or patterning in viscoelastic substrates were noted when internal pressure generated inside organoids was pharmacologically altered (Supplementary Fig. 14). To further test the ability of viscoelasticity to control organ growth, organoid development was monitored in matrices of varying stiffness. The percentage of Lgr5⁺ organoids and the number of colonies were higher in viscoelastic matrices compared with than elastic matrices, independent of G' (Fig. 6h,i). Increasing the G' of viscoelastic matrices again led to greater growth of intestinal organoids, symmetry breaking and finger formation, but organoids grew more slowly and maintained their spherical symmetry in elastic matrices (Fig. 6j–l and Supplementary Fig. 15). Overall, our simulations of organoid growth in six different matrix conditions are consistent with our experimental observations (Supplementary Fig. 16). Similarly to mammary epithelial spheroids, when the Arp2/3 complex, FAK or cell proliferation was inhibited, organoid symmetry breaking and budding were impaired (Supplementary Figs. 17b,c and 18). However, YAP was mainly in the cytoplasm in cells in buds in control organoids in viscoelastic matrices (Supplementary Fig. 17a). Simulations in which cell mobility or cell proliferation was inhibited similarly predicted a loss of organoid growth and symmetry breaking (Supplementary Figs. 19 and 20). In the model, we also found that the location of symmetry breaking is directly correlated to the location of the cells with relatively higher proliferation or motility (Supplementary Figs. 21–23). Overall, these results validate the theoretical model and the generality of the role of matrix viscoelasticity in tissue spatiotemporal organization.

Fig. 6 | Matrix viscoelasticity controls intestinal organoid growth, symmetry breaking, budding and cell patterning. **a**, Schematic depicting IPNs of alginate and Matrigel used in organoid studies. Viscoelasticity is controlled by polymer molecular weight and crosslinker concentration, while the concentration of Matrigel is maintained constant. **b**, Storage moduli of the elastic and viscoelastic alginate–Matrigel IPNs. $n = 6$ gels per condition. Statistical analysis was performed using a two-sided Mann–Whitney U -test. **c**, Representative examples of phalloidin and Hoechst stainings of intestinal organoids in elastic and viscoelastic hydrogels over 7 days of culture. Cyan, phalloidin; magenta, Hoechst. **d**, **e**, Quantification of the organoid area (**d**) and circularity (**e**) over 7 days in elastic and viscoelastic matrices. Error bars, s.e.m. $n = 24/26, 2/24, 27/22, 31/21, 19/23, 22/29, 21/26$ organoids in elastic/viscoelastic gels per day. **f**, Example of Lgr5⁺, phalloidin and Hoechst staining of intestinal organoids in a stiff viscoelastic gel after 7 days. Left: Lgr5⁺ (magenta) and Hoechst (cyan); right: phalloidin. **g**, Example of lysozyme, phalloidin and Hoechst staining of intestinal organoids in a stiff viscoelastic gel after 7 days. $n = 9$ images

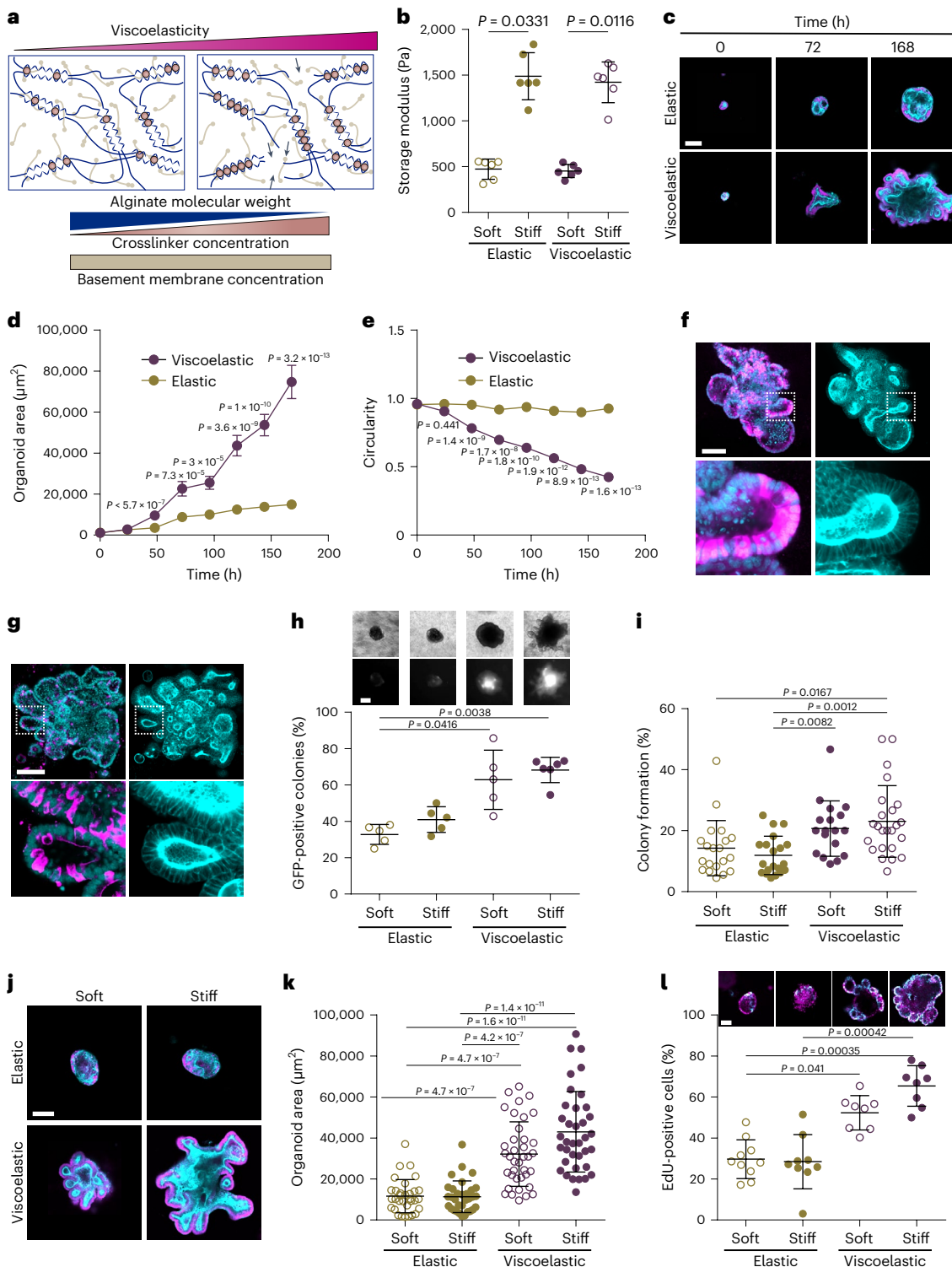
per condition. Left: lysozyme (magenta) and Hoechst (cyan); right: phalloidin. **h**, Representative examples of phase-contrast and Lgr5⁺ GFP images (upper row) and quantification of GFP-positive Lgr5⁺ intestinal organoids in soft and stiff viscoelastic and elastic matrices. $n = 5, 5, 5, 6$ samples per condition. **i**, Quantification of the percentage of colony formation per condition. $n = 20, 20, 18, 24$ images per condition. **j**, Examples of phalloidin (cyan) and Hoechst (magenta) stainings of intestinal organoids in soft and stiff elastic and viscoelastic matrices after 7 days. **k**, Quantification of the organoid area in soft and stiff elastic and viscoelastic matrices. $n = 32, 32, 38, 37$ organoids per condition. **l**, Example of EdU (cyan) and Hoechst (magenta) (upper row) and the percentage of EdU-positive cells (lower row) of intestinal organoids in soft and stiff elastic and viscoelastic matrices. $n = 10, 9, 8, 8$ organoids per condition. Statistical analysis was performed using a Kruskal–Wallis test followed by a post hoc Dunn's test except where indicated. All data are mean \pm s.d. except where indicated. Scale bars, 100 μ m.

Outlook

Our experiments and simulations demonstrate the passive properties of viscoelastic extracellular matrices as regulators of spatiotemporal tissue organization. The resulting morphology is reminiscent of interfacial instabilities in passively driven physical systems but modified fundamentally in living systems by the active processes of cell motility and proliferation that can destabilize the interface and are relevant to a number of processes, including embryogenesis^{9,37}, oncogenesis^{1,38}, branching morphogenesis⁴ and angiogenesis³⁹.

More broadly, our results are consistent with observations that the increase in ECM fluidity of the mesenchyme drives normal embryonic

airway branching⁴⁰, and an increase in tissue fluidity drives wound healing⁴¹, tissue elongation³⁴ or neural crest development⁴². Furthermore, invasive fingers are characterized by either an increase in matrix fluidity, as observed in glioblastoma⁴³, breast⁴⁴ and liver cancer⁴⁵ (compared to benign lesions and healthy ECM), or an increase in tissue fluidity, as tumour single cells are less viscous⁴⁶ and tumour tissues acquire more liquid-like properties⁴⁷⁻⁴⁹ (for example, EMT, unjamming). The increased expression of low-molecular-weight hyaluronic acid in malignant tumours⁵⁰ can explain the decrease in tumour ECM viscosity. Our results also suggest that when tumours migrate and grow and push the stroma, this may lead to the passive generation of stroma fingers in



the healthy tissue, as the stroma has more liquid-like properties than healthy tissue^{43–45}. Furthermore, our studies highlight the synergistic, but different, effect of viscoelasticity and stiffness in tissue spatiotemporal organization. Tissue growth and instability were observed in all of the viscoelastic gels used in these studies, with the stiffness of these gels impacting the extent of these behaviours. In purely elastic gels, however, altering the stiffness had minimal impact as tissue growth remained slow and stable. Finally, in addition to providing a framework to understand tissue morphology and organization in normal and pathological states, our study yields a phase diagram that might provide a strategy to guide tissue morphology in regenerative medicine.

Online content

Any methods, additional references, Nature Portfolio reporting summaries, source data, extended data, supplementary information, acknowledgements, peer review information; details of author contributions and competing interests; and statements of data and code availability are available at <https://doi.org/10.1038/s41563-022-01400-4>.

References

- Paszek, M. J. et al. Tensional homeostasis and the malignant phenotype. *Cancer Cell* **8**, 241–254 (2005).
- Sato, T. et al. Single Lgr5 stem cells build crypt-villus structures in vitro without a mesenchymal niche. *Nature* **459**, 262–265 (2009).
- Moris, N. et al. An in vitro model of early anteroposterior organization during human development. *Nature* **582**, 410–415 (2020).
- Hannezo, E. & Simons, B. D. Multiscale dynamics of branching morphogenesis. *Curr. Opin. Cell Biol.* **60**, 99–105 (2019).
- Nelson, C. M. On Buckling morphogenesis. *J. Biomech. Eng.* **138**, 021005 (2016).
- Briggs, J. A. et al. The dynamics of gene expression in vertebrate embryogenesis at single-cell resolution. *Science* **360**, eaar5780 (2018).
- Hannezo, E. & Heisenberg, C. P. Mechanochemical feedback loops in development and disease. *Cell* **178**, 12–25 (2019).
- Green, J. B. & Sharpe, J. Positional information and reaction–diffusion: two big ideas in developmental biology combine. *Development* **142**, 1203–1211 (2015).
- Chan, C. J. et al. Hydraulic control of mammalian embryo size and cell fate. *Nature* **571**, 112–116 (2019).
- Nelson, C. M. et al. Microfluidic chest cavities reveal that transmural pressure controls the rate of lung development. *Development* **144**, 4328–4335 (2017).
- Shyer, A. E., Huycke, T. R., Lee, C., Mahadevan, L. & Tabin, C. J. Bending gradients: how the intestinal stem cell gets its home. *Cell* **161**, 569–580 (2015).
- Harris, A. R. et al. Characterizing the mechanics of cultured cell monolayers. *Proc. Natl Acad. Sci. USA* **109**, 16449–16454 (2012).
- Barriga, E. H., Franze, K., Charras, G. & Mayor, R. Tissue stiffening coordinates morphogenesis by triggering collective cell migration in vivo. *Nature* **554**, 523–527 (2018).
- Thompson, A. J. et al. Rapid changes in tissue mechanics regulate cell behaviour in the developing embryonic brain. *Elife* **8**, e39356 (2019).
- Chaudhuri, O., Cooper-White, J., Janmey, P. A., Mooney, D. J. & Shenoy, V. B. Effects of extracellular matrix viscoelasticity on cellular behaviour. *Nature* **584**, 535–546 (2020).
- Elosegui-Artola, A. The extracellular matrix viscoelasticity as a regulator of cell and tissue dynamics. *Curr. Opin. Cell Biol.* **72**, 10–18 (2021).
- Heisenberg, C. P. & Bellaïche, Y. Forces in tissue morphogenesis and patterning. *Cell* **153**, 948–962 (2013).
- Debnath, J., Muthuswamy, S. K. & Brugge, J. S. Morphogenesis and oncogenesis of MCF-10A mammary epithelial acini grown in three-dimensional basement membrane cultures. *Methods* **30**, 256–268 (2003).
- Lee, K. Y. & Mooney, D. J. Alginate: properties and biomedical applications. *Prog. Polym. Sci.* **37**, 106–126 (2012).
- Chaudhuri, O. et al. Hydrogels with tunable stress relaxation regulate stem cell fate and activity. *Nat. Mater.* **15**, 326–334 (2016).
- Rowley, J. A., Madlambayan, G. & Mooney, D. J. Alginate hydrogels as synthetic extracellular matrix materials. *Biomaterials* **20**, 45–53 (1999).
- Elosegui-Artola, A. et al. Mechanical regulation of a molecular clutch defines force transmission and transduction in response to matrix rigidity. *Nat. Cell Biol.* **18**, 540–548 (2016).
- Lee, J. Y. et al. YAP-independent mechanotransduction drives breast cancer progression. *Nat. Commun.* **10**, 1848 (2019).
- Yang, J. et al. Guidelines and definitions for research on epithelial–mesenchymal transition. *Nat. Rev. Mol. Cell Biol.* **21**, 341–352 (2020).
- Taubenberger, A. V. et al. 3D microenvironment stiffness regulates tumor spheroid growth and mechanics via p21 and ROCK. *Adv. Biosyst.* **3**, 1900128 (2019).
- Wang, C., Tong, X. & Yang, F. Bioengineered 3D brain tumor model to elucidate the effects of matrix stiffness on glioblastoma cell behavior using PEG-based hydrogels. *Mol. Pharm.* **11**, 2115–2125 (2014).
- Saffman, P. G. & Taylor, G. I. The penetration of a fluid into a porous medium or Hele–Shaw cell containing a more viscous liquid. *Proc. R. Soc. Lond. A* **245**, 312–329 (1958).
- Biggins, J. S., Saintyves, B., Wei, Z., Bouchaud, E. & Mahadevan, L. Digital instability of a confined elastic meniscus. *Proc. Natl Acad. Sci. USA* **110**, 12545–12548 (2013).
- Shaebani, M. R., Wysocki, A., Winkler, R. G., Gompper, G. & Rieger, H. Computational models for active matter. *Nat. Rev. Phys.* **2**, 181–199 (2020).
- Berthier, L. & Kurchan, J. Non-equilibrium glass transitions in driven and active matter. *Nat. Phys.* **9**, 310–314 (2013).
- Lee, H.-p et al. The nuclear piston activates mechanosensitive ion channels to generate cell migration paths in confining microenvironments. *Sci. Adv.* **7**, eabd4058 (2021).
- Nam, S. et al. Cell cycle progression in confining microenvironments is regulated by a growth-responsive TRPV4-PI3K/Akt-p27(Kip1) signaling axis. *Sci. Adv.* **5**, eaaw6171 (2019).
- Ulrich, T. A., de Juan Pardo, E. M. & Kumar, S. The mechanical rigidity of the extracellular matrix regulates the structure, motility, and proliferation of glioma cells. *Cancer Res.* **69**, 4167–4174 (2009).
- Mongera, A. et al. A fluid-to-solid jamming transition underlies vertebrate body axis elongation. *Nature* **561**, 401–405 (2018).
- Chaudhuri, O. et al. Extracellular matrix stiffness and composition jointly regulate the induction of malignant phenotypes in mammary epithelium. *Nat. Mater.* **13**, 970–978 (2014).
- Gjorevski, N. et al. Designer matrices for intestinal stem cell and organoid culture. *Nature* **539**, 560–564 (2016).
- Deglincerti, A. et al. Self-organization of the in vitro attached human embryo. *Nature* **533**, 251–254 (2016).
- Friedl, P., Locker, J., Sahai, E. & Segall, J. E. Classifying collective cancer cell invasion. *Nat. Cell Biol.* **14**, 777–783 (2012).
- Lamallice, L., Le Boeuf, F. & Huot, J. Endothelial cell migration during angiogenesis. *Circ. Res.* **100**, 782–794 (2007).
- Spurlin, J. W. et al. Mesenchymal proteases and tissue fluidity remodel the extracellular matrix during airway epithelial branching in the embryonic avian lung. *Development* **146**, dev175257 (2019).

41. Tetley, R. J. et al. Tissue fluidity promotes epithelial wound healing. *Nat. Phys.* **15**, 1195–1203 (2019).
42. Kuriyama, S. et al. In vivo collective cell migration requires an LPAR2-dependent increase in tissue fluidity. *J. Cell Biol.* **206**, 113–127 (2014).
43. Streitberger, K. J. et al. How tissue fluidity influences brain tumor progression. *Proc. Natl Acad. Sci. USA* **117**, 128–134 (2020).
44. Sinkus, R. et al. Viscoelastic shear properties of in vivo breast lesions measured by MR elastography. *Magn. Reson. Imaging* **23**, 159–165 (2005).
45. Shahryari, M. et al. Tomoelastography distinguishes non-invasively between benign and malignant liver lesions. *Cancer Res., canres.* **2150**, 2019 (2019).
46. Nematbakhsh, Y., Pang, K. T. & Lim, C. T. Correlating the viscoelasticity of breast cancer cells with their malignancy. *Converg. Sci. Phys. Oncol.* **3**, 034003 (2017).
47. Palamidessi, A. et al. Unjamming overcomes kinetic and proliferation arrest in terminally differentiated cells and promotes collective motility of carcinoma. *Nat. Mater.* **18**, 1252–1263 (2019).
48. Han, Y. L. et al. Cell swelling, softening and invasion in a three-dimensional breast cancer model. *Nat. Phys.* **16**, 101–108 (2020).
49. Staneva, R. et al. Cancer cells in the tumor core exhibit spatially coordinated migration patterns. *J. Cell Sci.* **132**, jcs220277 (2019).
50. Monslow, J., Govindaraju, P. & Puré, E. Hyaluronan—a functional and structural sweet spot in the tissue microenvironment. *Front. Immunol.* **6**, 231 (2015).

Publisher's note Springer Nature remains neutral with regard to jurisdictional claims in published maps and institutional affiliations.

Springer Nature or its licensor (e.g. a society or other partner) holds exclusive rights to this article under a publishing agreement with the author(s) or other rightsholder(s); author self-archiving of the accepted manuscript version of this article is solely governed by the terms of such publishing agreement and applicable law.

© The Author(s), under exclusive licence to Springer Nature Limited 2022

Methods

Alginate hydrogel preparation

Sodium alginate with an average molecular weight of 138 kDa (high molecular weight) was purchased from FMC Biopolymer (Protanal LF10/60) and used to prepare more elastic and viscoelastic gels as described previously^{20,21}. Briefly, alginate was irradiated with a 5 mrad cobalt source to obtain a low-molecular-weight alginate (38 kDa). The adhesion peptide GGGGRGDSP (RGD, Peptide 2.0) was covalently coupled to alginate (RGD concentration, 2.7 mM) utilizing carbodiimide chemistry (Sulfo-NHS, Pierce Chemical; EDC, Sigma-Aldrich). Lissamine rhodamine B ethylenediamine (ThermoFisher) was also coupled to alginate using carbodiimide chemistry for experiments involving fluorescent alginate as described previously³⁵. Next, modified alginate was dialysed against deionized water for 3–4 days (molecular weight cutoff, 3.5 kDa), treated with activated charcoal (Sigma-Aldrich), filter sterilized (0.22 μm) and lyophilized for 1 week. The day before the experiment, alginate was reconstituted in DMEM/F12 (Dulbecco's modified Eagle's medium: Nutrient Mixture F12, Gibco). For the MCF10A spheroid experiments, two syringes per gel were prepared to obtain a 2% alginate gel: one contained 2.5% alginate; the second syringe contained normal medium and different amounts of calcium sulfate depending on the material mechanical properties. Calcium sulfate was previously diluted in media without supplements. Then, spheroids were gently added to the syringe with media and the syringe was turned up and down to thoroughly mix the calcium sulfate. Next, both syringes were connected together with a female–female Luer-lock coupler, taking care not to introduce bubbles or air into the mixture. The two solutions were then mixed rapidly, and the alginate gel was immediately deposited on top of a plate. The recipes for all alginate hydrogels were the same except for the calcium sulfate concentration which was increased to increase the stiffness: 16.8, 28.8, 57.6, 82.4 mM and 33.6, 52.8, 96, 163.6 mM for elastic and viscoelastic hydrogels, respectively. For the intestinal organoid experiments, gels were prepared differently. First, the alginate and Matrigel solution was prepared. Alginate and Matrigel were left on ice for over 1 h. Next, Matrigel was added to a 2.5% alginate solution. As Matrigel concentration varies from batch to batch, the appropriate amount of media (with no supplements) was added to a final concentration of 1.25% alginate and 5 mg ml⁻¹ Matrigel. This solution was thoroughly mixed 40–50 times with a pipette, being careful not to generate bubbles, and maintained in ice. First, a syringe with alginate–Matrigel solution was prepared and left on top of the ice. A second syringe was prepared with medium and the appropriate concentration of calcium sulfate. In parallel, Matrigel with organoids was dissolved with cell recovery solution. The recipes for all alginate–Matrigel hydrogels were the same except for the calcium sulfate concentration which increased to increase the stiffness: 26.4, 48, 72.6 mM and 48, 96, 163.6 mM for elastic and viscoelastic hydrogels, respectively.

Mechanical characterization of hydrogels

The storage moduli of hydrogels were determined with an AR-G2 stress-controlled rheometer (TA Instruments) as utilized previously^{20,51}. Briefly, a 20 mm parallel plate was used with a gap of 1 mm. The circular plate was immediately placed on the polymer solution before the hydrogel started to gel, forming a 20 mm disk hydrogel. Oscillatory rheology (1 Hz, 1% strain) was used to measure the storage modulus. Gels were maintained at 37 °C until equilibrium was reached.

To measure the stress relaxation half-time a compression test with an Instron 3342 mechanical apparatus was performed as described previously^{20,52}. Briefly, hydrogels were fabricated with a 2 mm height, and allowed to equilibrate for 24 h^{51,53,54}. Then, gels were strained at a rate of 1 mm min⁻¹ until a 15% strain was reached; the strain was then held constant. The stress relaxation half-time was measured as the time at which the initial stress decreased by a factor of 2.

MCF10A cell culture

The MCF10A breast cell line (ATCC, CRL-10317) was cultured following the protocols developed by Debnath and Brugge¹⁸. Briefly, cells were cultured in DMEM/F12 media (Gibco) supplemented with 5% horse serum (Invitrogen), 1% penicillin/streptomycin (Invitrogen), 20 ng ml⁻¹ epidermal growth factor (Peprotech), 0.5 mg ml⁻¹ hydrocortisone (Sigma-Aldrich), 100 ng ml⁻¹ cholera toxin (Sigma-Aldrich) and 10 $\mu\text{g ml}^{-1}$ insulin (Sigma-Aldrich).

MCF10A spheroid experiments

To prepare MCF10A spheroids, cells were trypsinized from tissue culture flasks and resuspended in pretreated Aggrewell multiwell plates (Aggrewell 400) to generate spheroids of ~2,000 cells. Plates were left overnight in the incubator to allow spheroids to form. The spheroids were then carefully removed from the Aggrewell plates and added to the polymer solution before gelation (see Alginate hydrogel preparation above). A plate was deposited on top of each gel to provide a final controlled height of 1 mm, and gels were left in the incubator for 45 min. Individual gel samples were then obtained with an 8 mm puncher, and each gel was introduced into a separate well of a 24-well plate. The media was changed after 2 h, and during experiments the media was changed every 2 days, except where indicated. For experiments with inhibitors, once spheroids were encapsulated in gels and gels equilibrated, media with the defined inhibitor concentration was added. The media with inhibitors was also changed every 2 days. The inhibitors used were: 10 μM Y27632 (Sigma-Aldrich) to inhibit ROCK, 50 μM NSC23766 (TOCRIS) to inhibit Rac1, 100 μM CK666 to inhibit ARP 2/3, 10 μM gadolinium to block ion channels, 5 μM PF 573228 (TOCRIS) to inhibit FAK, 2 mM thymidine (Sigma-Aldrich) to block cell cycle progression and 20 μM SMIFH2 (Sigma-Aldrich) to inhibit formin.

Intestinal organoid culture

Intestinal organoids were cultured from isolated jejunal crypts of Lgr5^{CreER^{GFP}} adult mice (Jackson Laboratory) in which the Lgr5⁺ stem cells are labelled with GFP expression. Intestinal organoids were cultured in DMEM/F12 media (Invitrogen) supplemented with 10% RS2 condition medium (RS2 producer line was a gift from Dr Xi He, Boston Children's Hospital), 10 mM HEPES (ThermoFisher), 1 \times GlutaMAX supplement (ThermoFisher), 1 \times N2 supplement (ThermoFisher), 1 \times B27 supplement (ThermoFisher), 10 μM DMH1 (Cayman), 20 μM CHIR99021 (LC Laboratories), 50 ng ml⁻¹ epidermal growth factor (R&D), 10 μM Y27632 (LC Laboratories) and 0.1 mg ml⁻¹ Primocin (invivoGen). For routine culture, medium was changed every 2–3 days and organoids were passaged after 5 days at the latest. To passage the organoids, cell recovery solution (Corning) was added to the wells containing intestinal organoids in Matrigel (Corning) to disrupt Matrigel. After adding the cell recovery solution, the plate was left on ice until Matrigel was degraded. Then, organoids were gently disrupted using mechanical agitation. Disrupted organoids were added to a Matrigel-containing solution and 30 μl droplets of Matrigel with organoids were deposited in preheated wells. These wells were left in an incubator for 30 min to allow Matrigel to solidify and before adding medium.

Intestinal organoid experiments

Intestinal organoid encapsulation was similar to the procedure utilized for MCF10A spheroids, although in this case an interpenetrating network (IPN) of alginate and Matrigel was used for encapsulation. Intestinal organoids were first cultured in Matrigel (BD Biosciences) for 1–2 weeks. Then, the Matrigel was dissolved with cell recovery solution (Corning) and organoids were dissociated with TrypLE (Gibco). After dissociation, cells were encapsulated in Matrigel for 24 h. This process allows the size of organoids to be more homogeneous at the start of the experiment. After 24 h, organoids were added to the syringe with Matrigel–alginate prior to gel formation. To control the thickness of the gels, a plate was deposited on top of each gel at a controlled height of

1 mm. Gels were allowed to form inside the incubators for 45 min, and individual gel samples were then punched with an 8 mm puncher. Each gel was introduced into a separate well of a 24-well plate. Medium was changed after 2 h, and subsequently every 2 days, except where indicated. For single-organoid experiments, organoids were dissociated and directly encapsulated in the Matrigel-alginate. For experiments with addition of 100 μ M ouabain (Sigma-Aldrich), media with ouabain was added after equilibration and was changed every day.

Bulk hydrogel immunostaining

Hydrogels were fixed with 4% paraformaldehyde for 30 min. After fixation, hydrogels were washed with PBS with 10 mM EDTA to facilitate staining. Then, cells within hydrogels were permeabilized and blocked with 0.5% Triton, 3% goat serum in PBS with calcium (blocking buffer) for 24 h. Once hydrogels were permeabilized and blocked, primary antibodies were added in blocking buffer for 24 h. Primary antibodies used were YAP (Santa Cruz, 1:200), cytokeratin 14 (Covance, 1:100) and vimentin (abcam, 1:200). After incubation with primary antibodies, hydrogels were washed for 24 h in blocking buffer. Next, secondary antibodies were added in blocking buffer. Then, hydrogels were washed for 3 h and blocking buffer with phalloidin (ThermoFisher, 1:200) was then added for 24 h to label F-actin. Hydrogels were then washed for 8 h with blocking buffer with Hoechst (ThermoFisher, 1:2,000) to label cell nuclei, and afterwards washed with PBS overnight. Finally, Prolong (ThermoFisher) antifade reagent was added to the hydrogels.

Immunostaining of hydrogel sections

Hydrogels were fixed with 4% paraformaldehyde for 30 min. After fixation, hydrogels were washed three times with PBS containing calcium (cPBS), and then incubated overnight in cPBS containing 30% sucrose. Hydrogels were then incubated in a solution consisting of equal volumes of a solution of 30% sucrose in cPBS and OCT solution (Tissue-Tek) for 24 h. Next, the solution was removed and hydrogels were embedded in OCT for several hours, and then frozen. The frozen hydrogels were sectioned with a cryostat (Leica CM1950) to a thickness of 15 μ m. Sections were permeabilized with a PBS solution containing 0.2% Triton and 3% goat serum. Next, pFAK (abcam, 1:100), emerin (Santa Cruz, 1:100) or nesprin (ThermoFisher, 1:100) antibody was added for 3 h. Then, after six washes, a secondary antibody with phalloidin was added for 1 h. Last, ProLong (ThermoFisher) antifade reagent was added. After mounting, sections were imaged with 20 \times (numerical aperture (NA), 0.8), 40 \times (NA, 1.0) or 63 \times (NA, 1.4) water immersion objectives in an upright laser-scanning confocal Zeiss LSM 710.

Bulk organoid staining

To follow the 3D structure and evolution of organoids, the F-actin and nuclei were stained with phalloidin and Hoechst, respectively. Hydrogels were fixed with 4% paraformaldehyde for 30 min. After fixation, hydrogels were washed with PBS containing 10 mM EDTA to facilitate staining. Then, hydrogels were permeabilized and blocked with 0.5% Triton and 3% goat serum in PBS with calcium (blocking buffer) for 48 h. Once hydrogels were permeabilized and blocked, phalloidin (ThermoFisher, 1:200) was added to blocking buffer to label F-actin and incubated with gels for 24 h. Hydrogels were then washed for 8 h with blocking buffer with Hoechst (ThermoFisher, 1:2,000) to label the nuclei, and then washed with PBS overnight. Finally, Prolong (ThermoFisher) antifade reagent was added to the hydrogels. After mounting, organoids were imaged with a 40 \times (NA, 1.0) water immersion objective in an upright laser-scanning confocal Zeiss LSM 710.

Organoid immunostaining

Hydrogels were incubated in cell recovery solution (Corning) for 45 min on ice. The alginate in the gels was then degraded with 34 U ml⁻¹ alginate lyase (Sigma-Aldrich), while maintaining gels on ice. Hydrogels were subsequently fixed with 4% paraformaldehyde for 30 min. After

fixation, organoids were permeabilized for 30 min with 0.5% Triton. Once organoids were permeabilized, they were blocked with 3% goat serum and 0.1% Triton in PBS for 3 h. Then, primary antibodies lysozyme (Dako, 1:200), L-FABP (Santa Cruz, 1:50), Chromogranin A (Santa Cruz, 1:50), Sox9 (Abcam, 1:50), Mucin 2 (ThermoFisher, 1:50) were added in 3% goat serum and 0.1% Triton in PBS and left overnight at 4 °C. Once the primary antibody was washed the next day, secondary antibodies (ThermoFisher, 1:200) and phalloidin (ThermoFisher, 1:200) were added to gels in a solution containing 3% goat serum and 0.1% Triton in PBS for 4 h. Secondary antibodies were then washed, organoids were incubated with Hoechst (ThermoFisher, 1:2,000) for 4 h, washed six times, and finally ProLong (ThermoFisher) was added. After mounting, organoids were imaged with a 40 \times (NA, 1.0) water immersion objective in a laser-scanning confocal upright Zeiss LSM 710.

Analysis of cell proliferation in tissues

In experiments with MCF10A spheroids, EdU (Click-iT EdU Cell Proliferation Kit, Invitrogen) was added for 4 h to spheroids containing bulk hydrogels at day 5. For intestinal organoid experiments, EdU was added for 2 h at day 7. After following the staining protocol provided by Invitrogen, ProLong mounting media was added. After mounting, spheroids or organoids were imaged with a 20 \times (NA, 0.8) or a 40 \times (NA, 1.0) water immersion objective in an upright laser-scanning confocal Zeiss LSM 710. The percentage of EdU-positive cells was quantified by determining the total number of cells from the Hoechst channel, and then the number of EdU-positive nuclei. Custom MATLAB software was used to quantify the spatial distribution of EdU-positive cells and cell density across the spheroids. In brief, the perimeter of a 2D slice of a spheroid was first defined. Then, the tissue area was divided into squares of defined area. To measure the local density and the percentage of EdU-positive cells, the software measures the number of nuclei from the Hoechst staining and the number of EdU-positive nuclei per square. With these measurements, the local density of cells and the percentage of EdU-positive cells are calculated. The radial distribution of cell density and percentage of EdU-positive cells was also quantified. To accomplish this, the distance from the centre to the edge of the tissue was normalized to compare all spheroids and conditions.

Spheroid area and circularity quantification

To measure spheroid or organoid circularity and area during the experiments, phase-contrast images were taken with 4 \times and 10 \times objectives with a microscope (EVOS) every day or the last day of the experiments. These images were quantified with Image J. Briefly, the perimeter of each individual spheroid/organoid was drawn manually, and the enclosed area and circularity was measured.

Cytokeratin 14 quantification

To measure cytokeratin 14 staining intensity, images were obtained after immunostaining with a 20 \times (NA, 0.8) or a 40 \times (NA, 1.0) water immersion objective in an upright laser-scanning confocal Zeiss LSM 710. Then, custom MATLAB software was used to quantify the average intensity of the cytokeratin 14 staining per spheroid. First, the perimeter of each spheroid was defined. Then, the perimeter ring width was widened inwards and outwards to include all pixels positive for cytokeratin 14 staining. The average cytokeratin 14 intensity was then determined, and all values were normalized to the average value of cytokeratin 14 staining in elastic hydrogels.

YAP quantification

To quantify YAP staining, images of immunostained spheroids were taken with a 100 \times (NA, 1.40) oil immersion objective using a laser-scanning confocal upright Zeiss LSM 710. The percentage of cells with nuclear YAP was quantified by counting the number of cells with nuclear YAP with respect to the total number of cells. These

measurements were performed in the core of spheroids, the edges and cells present at the initiation of fingers (in viscoelastic gels).

Mice experiments with MDA-MB-231 cells

Female, 3-week-old NOD SCID mice (NOD.Cg-Prkdc^{scid}/J) were purchased from Jackson Laboratory. MDA-MB-231 cells (1×10^7 cells ml⁻¹) were added to alginate solutions (hydrogel preparation was performed as described above to yield the stiff viscoelastic and elastic gels), mixed and immediately injected subcutaneously at the left flank to allow gelation in situ. The dimensions of the growing tumours were measured externally using calipers, and the volume of an ellipsoid was calculated. All animal studies were performed in accordance with guidelines set by the National Institutes of Health and the Harvard University Faculty of Arts and Sciences' Institutional Animal Care and Use Committee (IACUC).

Microfluidic device development and cell-flux-driven experiments

To explore the impact of pressure on tissue growth, gels containing cell spheroids were confined by placing a polydimethylsiloxane (PDMS) cover over gels contained within a Petri dish. The PDMS cover was fabricated to allow continuous injection of a cell suspension into the centre of a spheroid to model pressure-driven tissue growth. The cover was fabricated by mixing PDMS (Sylgard 184, Dow Corning) base and crosslinker in a 5:1 weight ratio using a mixer (AR-100, Thinky). The PDMS was degassed for 20 min and the mould was cured in the oven at 65 °C overnight. The device was then cut out of the mould and a hole through the device was created with a 1.2 mm biopsy punch (Uni-Core, GE Healthcare Life Sciences). The alginate solution was kept at room temperature. The PDMS cover was then surfaced treated with Aquapel (PPG Industries) to make the gel-contacting surface hydrophobic. Once ready, hydrogel solution prepared as described above is poured onto a Petri dish of 100 mm diameter to allow gelation. Eight circular pillars were used to surround the forming hydrogel to control its thickness. Then, any remaining air bubbles were carefully removed with a pipette. The PDMS cover was then placed on top of the forming gel, supported by the pillars, to create gels ~170 µm thick. Hydrogels were allowed to cure at room temperature for 30 min. During this time, cells are stained (Hoechst nucleus stain, ThermoFisher), suspended in cell medium at a density of 1×10^7 cells ml⁻¹ and loaded into a syringe. Once the hydrogel has formed, the syringe pump was used to inject the cell suspension into the centre of the gel using a 200 mm length (L) tubing of radius (R) 0.2 mm inserted through the hole created in the PDMS cover. The tubing was cut parallel to the PDMS to favour even cell injection in all directions at a constant rate. Cells were injected for 9 min, at a flow rate, Q , of 1 µl min⁻¹, to provide a constant pressure of 19 kPa. We calculated the pressure from the Hagen–Poiseuille Law. The dynamic viscosity (μ) of MCF10A cells is ~0.01 Pa·s (ref. ⁵⁵).

$$\Delta P = \frac{8\mu L Q}{\pi R^4}$$

Mice experiments with MCF10A cells

Alginate gels (2 mm high, low or high molecular weight, stiff) containing MCF10A spheroids were prepared as previously described and 8-mm-diameter gels were obtained using a biopsy punch. Gels were surgically implanted in the subcutaneous space on the flanks of NU/J athymic nude mice. For histological analysis, gels were excised 7 days after implantation, fixed in 1% paraformaldehyde (Electron Microscopy Sciences) and transferred to a 30% sucrose solution overnight. Gels were then embedded in Tissue-Tek OCT compound (VWR) and sectioned to 20 µm on a Leica CM1950 cryostat. Sections were stained for vimentin (abcam, 1:200), phalloidin (ThermoFisher, 1:200), mitochondria (abcam, 1:200) and imaged using a Zeiss LSM 710 confocal microscope.

Flow cytometry of MCF10A cells from gels

Gels containing MCF10A spheroids were prepared as previously described. For flow cytometric analysis, gels from in vitro or in vivo experiments were collected and digested in MCF10A medium containing 1 mg ml⁻¹ alginate lyase (Sigma), 25 mM EDTA (Sigma) and 100 U ml⁻¹ collagenase IV (STEMCELL Technologies). Retrieved spheroids were incubated for 60 s in 0.05% Trypsin–EDTA (Gibco), passed through a 70 µm filter and counted using a Countess II FL (ThermoFisher). Single-cell suspensions were permeabilized and fixed using the eBioscience Foxp3/Transcription Factor Staining Buffer Set (Invitrogen) and stained with antibodies against human ZEB1, Snail, Slug and ZEB2 (R&D Systems). Cells were run on a BD LSR II flow cytometer and analysed using FlowJo v.10 software.

Characterization of interpenetration of alginate–Matrigel networks

To characterize the interpenetration, homogeneity and the lack of phase separation we followed the same procedure as described previously³⁵. We performed fluorescence microscopy of the IPNs to quantify the intensity distribution of alginate and Matrigel in the matrix. To study the intensity distribution of alginate, the intensity of fluorescently coupled rhodamine–alginate was analysed. To study the intensity distribution of Matrigel, immunostaining of laminin (abcam, 1:200) was performed. Images were acquired with a Zeiss LSM 710 confocal microscope. The distribution observed for all conditions in Supplementary Fig. 11 show a single peak. If phase separation occurred, there would be two or more peaks indicating different concentrations of alginate or laminin.

Scanning electron microscopy experiments

To prepare samples for scanning electron microscopy (SEM), the gels were first fixed in paraformaldehyde for 15 min and then rinsed three times with PBS with 10 mM CaCl₂. Next, the samples were dehydrated in increasing ethanol baths as follows: 50% ethanol, 50% deionized water ×1 change, 70% ethanol, 30% deionized water ×1 change, 80% ethanol, 20% deionized water ×2 changes, 90% ethanol, 10% deionized water ×2 changes, 100% ethanol ×2 changes. After the gels were left in the 100% ethanol bath, they were added to a 1:2 solution of hexamethyldisilazane (HMDS):ethanol for 20 min, then transferred to a 1:1 HMDS:ethanol solution for 20 min and finally left in a purely HMDS solution overnight. The lid of the container was left slightly ajar to allow the HMDS to evaporate. To prepare the samples for imaging, each sample was mounted to a SEM stub (Ted Pella) using conductive carbon tape. The samples were coated with 10 nm of Pt/Pd 80/20 using an EMS 150TS metal sputter coater (Quorum), and finally placed in a field emission SEM (FESEM Ultra55, Zeiss). The samples were imaged at 2–3 keV using the InLens SE detector.

Nanostring analysis

Three independent experiments were performed ($n = 3$). For each experiment, three gels per condition (technical replicates) were included and samples from each (taken with a biopsy punch) were pooled together to obtain RNA. Cells were retrieved from the gels by alginate lyase digestion and then lysed with RLT buffer (Qiagen) with 1% β-mercaptoethanol. RNA was isolated with an RNAeasy Mini Kit and on-column DNA digestion (Qiagen) following the manufacturer's instructions. RNA quantity and quality was initially determined with a spectrophotometer (Nanodrop) and confirmed by electrophoresis (Agilent TapeStation 4200). All samples included had excellent RNA integrity (RIN, ≥9.6). For each sample, 75 ng RNA was used for nanostring analysis (PanCancer Progression panel consisting of human 770 genes) following the manufacturer's recommendations. Raw data were analysed with Nsolver 4.0 software.

Reporting summary

Further information on research design is available in the Nature Portfolio Reporting Summary linked to this article.

Data availability

Digital data supporting the findings of this article are available at https://dataverse.harvard.edu/dataverse/EloseguiArtola_Gupta_2022. Source data are provided with this paper.

Code availability

The computational model code is available at https://github.com/anupamdata/ABM_VE_Matrix_Viscous_Tissue.git

References

51. Chaudhuri, O. et al. Substrate stress relaxation regulates cell spreading. *Nat. Commun.* **6**, 6364 (2015).
52. Darnell, M. et al. Material microenvironmental properties couple to induce distinct transcriptional programs in mammalian stem cells. *Proc. Natl Acad. Sci. USA* **115**, E8368–E8377 (2018).
53. Huebsch, N. et al. Harnessing traction-mediated manipulation of the cell/matrix interface to control stem-cell fate. *Nat. Mater.* **9**, 518–526 (2010).
54. Zhao, X., Huebsch, N., Mooney, D. J. & Suo, Z. Stress-relaxation behavior in gels with ionic and covalent crosslinks. *J. Appl. Phys.* **107**, 63509 (2010).
55. Corbin, E. A., Kong, F., Lim, C. T., King, W. P. & Bashir, R. Biophysical properties of human breast cancer cells measured using silicon MEMS resonators and atomic force microscopy. *Lab Chip* **15**, 839–847 (2015).

Acknowledgements

We thank M. Sobral, M. Dellacherie, J. Lou, M. Uroz and all the members of the Mooney lab for helpful discussions and comments on the manuscript. This work was supported by funding from the Wellcome Leap HOPE Program (D.J.M.). This project has received funding from the European Research Council (ERC) under the European Union's Horizon 2020 research and innovation programme (grant agreement number 851055) (A.E.-A.). A.E.-A. received funding

for this work from the European Union's Horizon 2020 research and innovation programme through a Marie Skłodowska-Curie grant agreement number 798504 (MECHANOSITY). A.J.N. acknowledges a Graduate Research Fellowship from the National Science Foundation. This work was partly supported by funding (R01 DK125817 and Tri-SCI grant) to Q.Z. I.d.L. was supported by the National Cancer Institute of the National Institutes of Health under award number U01CA214369. The content is solely the responsibility of the authors and does not necessarily represent the official views of the National Institutes of Health or the Wyss Institute for Biologically Inspired Engineering at Harvard University.

Author contributions

A.E.-A. and D.J.M. conceived the study. A.E.-A., A.J.N., B.R.S., R.G., C.M.T., I.d.L., D.A.W. and D.J.M. designed the experiments. A.E.-A., A.J.N., B.R.S., R.G., C.M.T., I.d.L. and M.D. performed the experiments. A.G. and L.M. developed the computational model. W.G. and Q.Z. provided reagents. A.E.-A., A.G., L.M. and D.J.M. wrote the manuscript.

Competing interests

The authors declare no competing interests.

Additional information

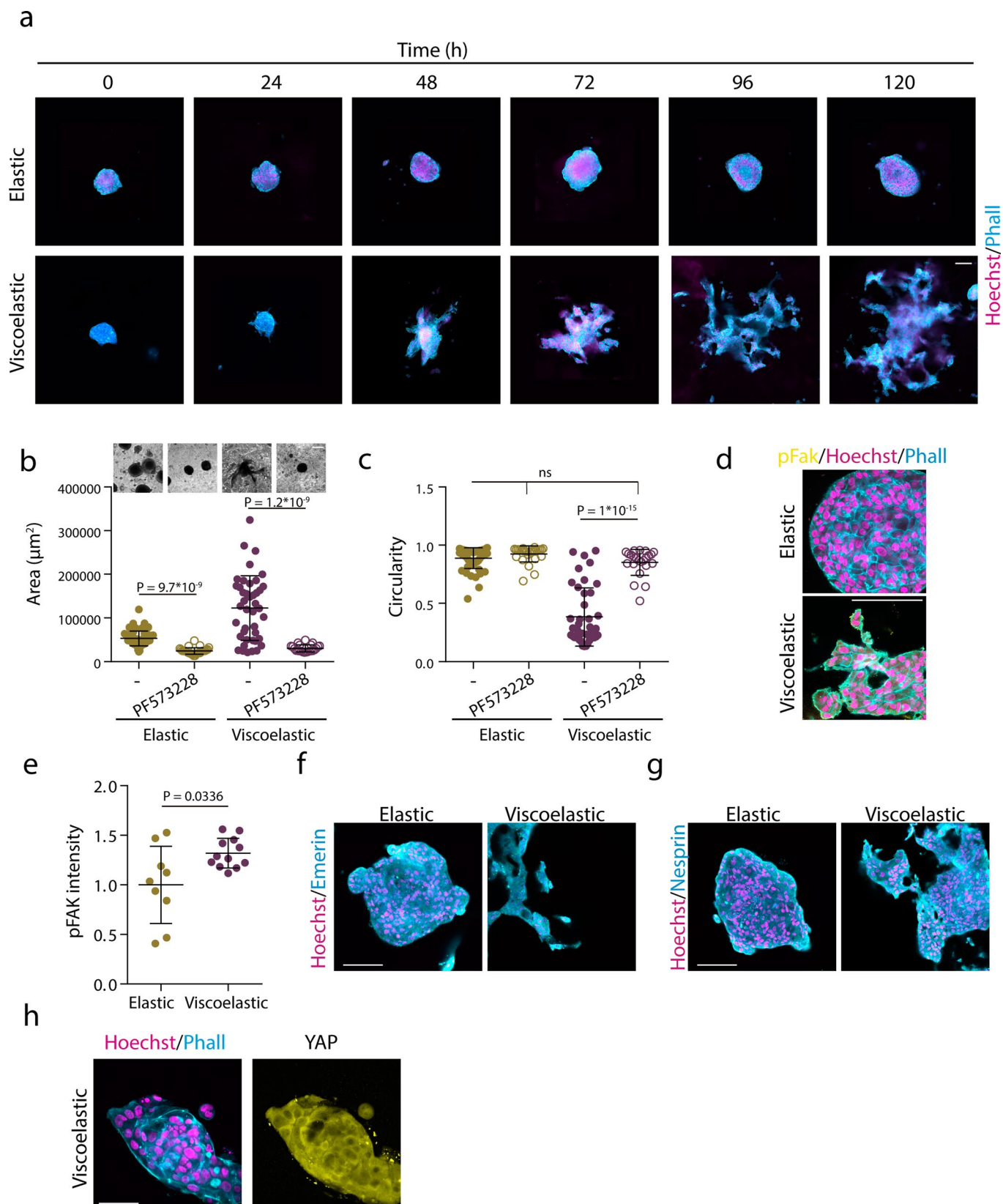
Extended data is available for this paper at <https://doi.org/10.1038/s41563-022-01400-4>.

Supplementary information The online version contains supplementary material available at <https://doi.org/10.1038/s41563-022-01400-4>.

Correspondence and requests for materials should be addressed to L. Mahadevan or David J. Mooney.

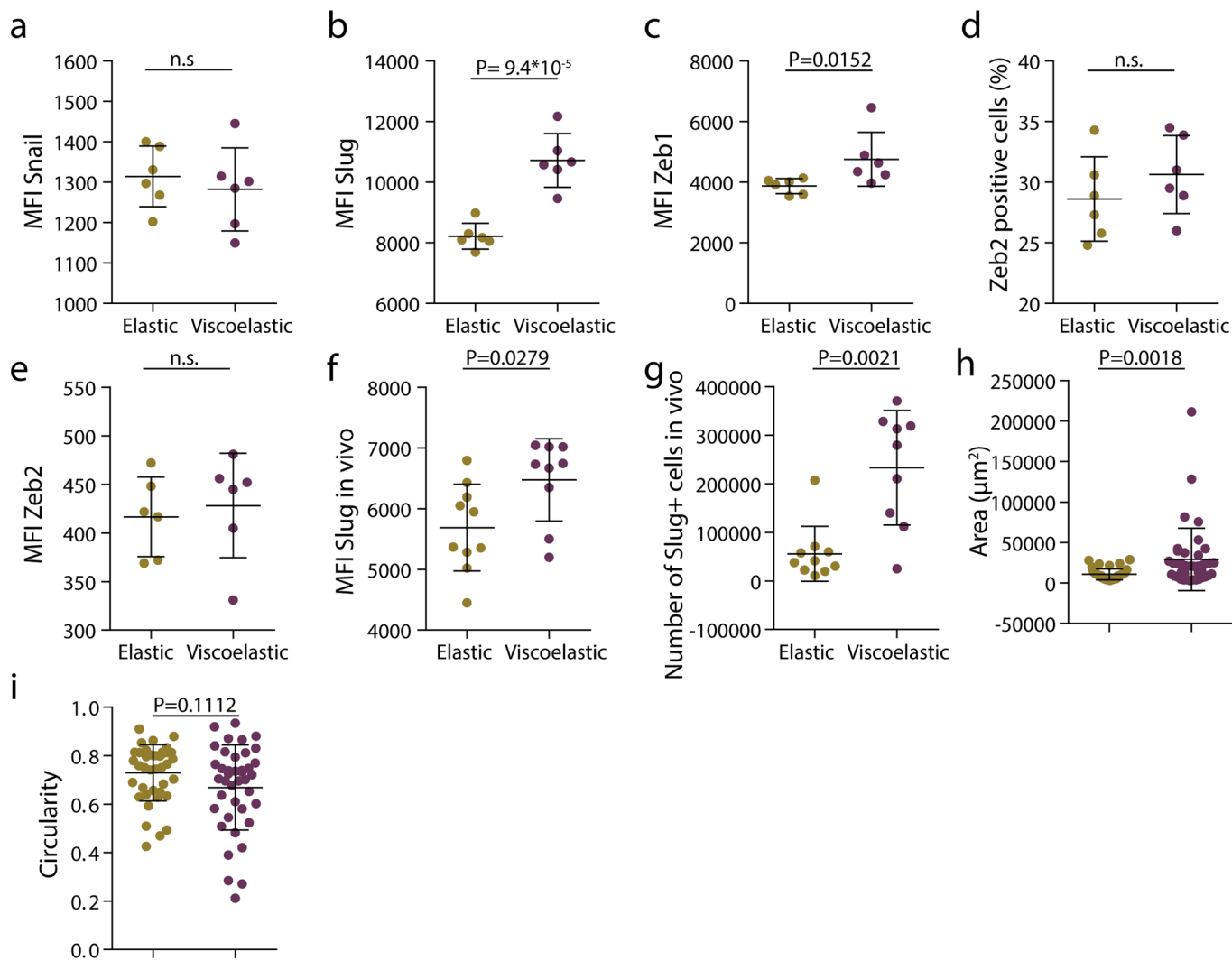
Peer review information *Nature Materials* thanks Nuria Montserrat and the other, anonymous, reviewer(s) for their contribution to the peer review of this work.

Reprints and permissions information is available at www.nature.com/reprints.



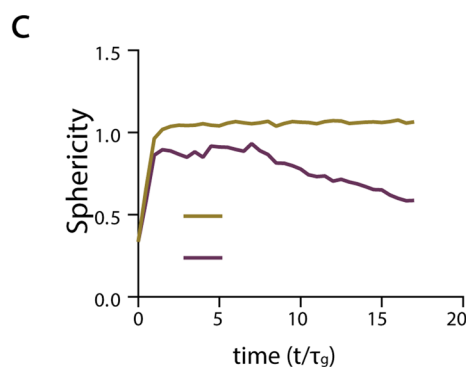
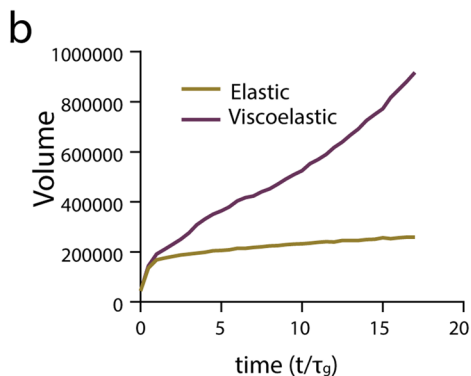
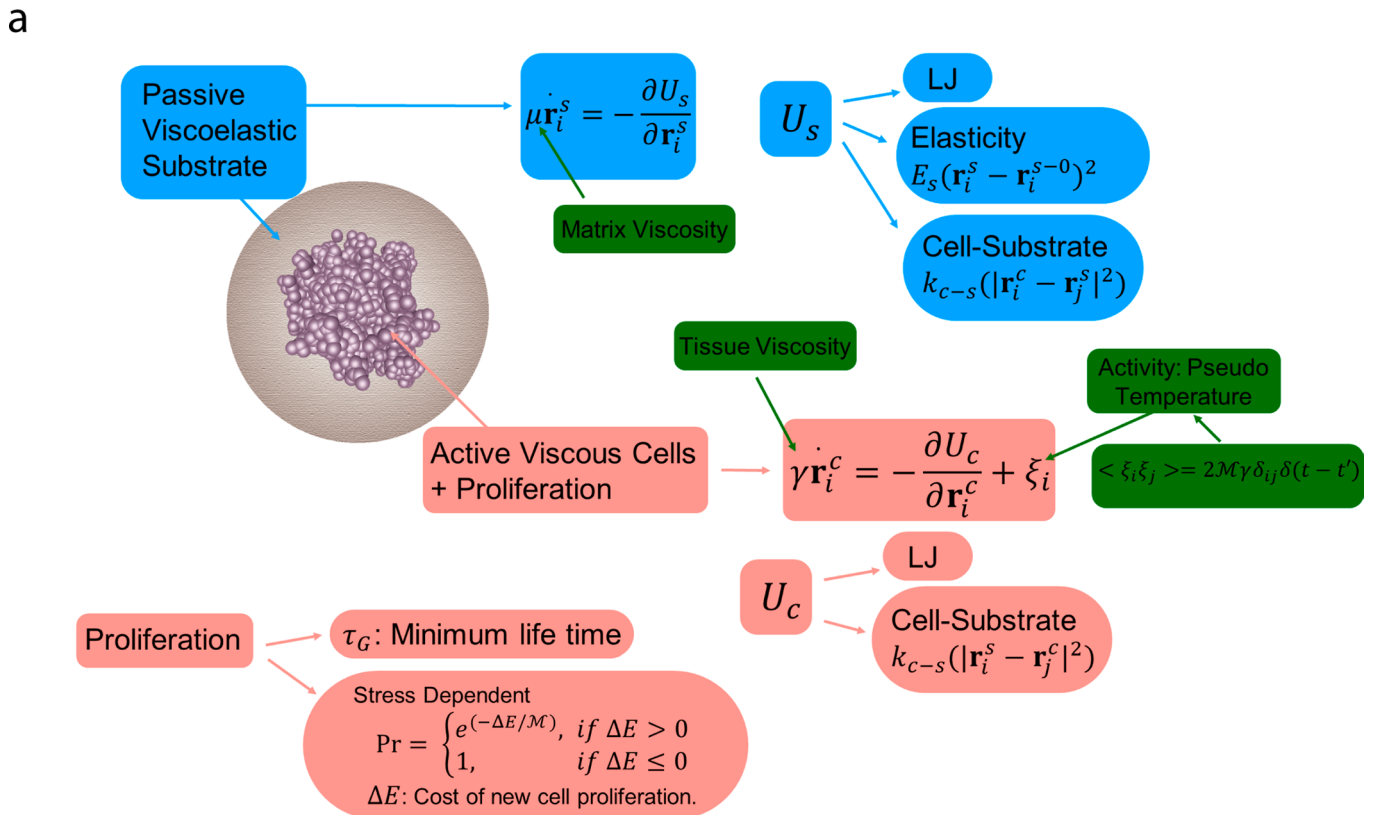
Extended Data Fig. 1 | Matrix Viscoelasticity regulates tissue growth and geometry. Examples of growth of MCF10A spheroids in elastic versus viscoelastic hydrogels over 5 days. Phalloidin in cyan, Hoechst in magenta. **b, c**, Quantification of spheroids area (**b**) and circularity (**c**) after 5 days without or with focal adhesion kinase (FAK) inhibitor PF 573228. $n = 56, 27, 41, 23$ spheroids per condition. Statistical analysis was performed using Kruskal–Wallis test followed by post hoc Dunn's test. **d, e**, Representative examples (**d**) and quantification of pFAK (**e**) in spheroids in elastic and viscoelastic matrices.

$n = 9, 12$ images per condition. Statistical analysis was performed using two-sided Mann-Whitney U-test. **f, g**, Representative examples of emerin and nesprin staining in elastic and viscoelastic matrices. $n = 15, 9$ (**f**) and $n = 14, 14$ images per condition. No significant differences were observed between cells in elastic and viscoelastic matrices. **h**, Representative examples of phalloidin, Hoechst (left) and YAP (right) stainings of spheroids with thymidine treatment of cells in viscoelastic gels. $n = 5$ images. All data represent mean \pm s.d.; all scale bars represent 100 μm .



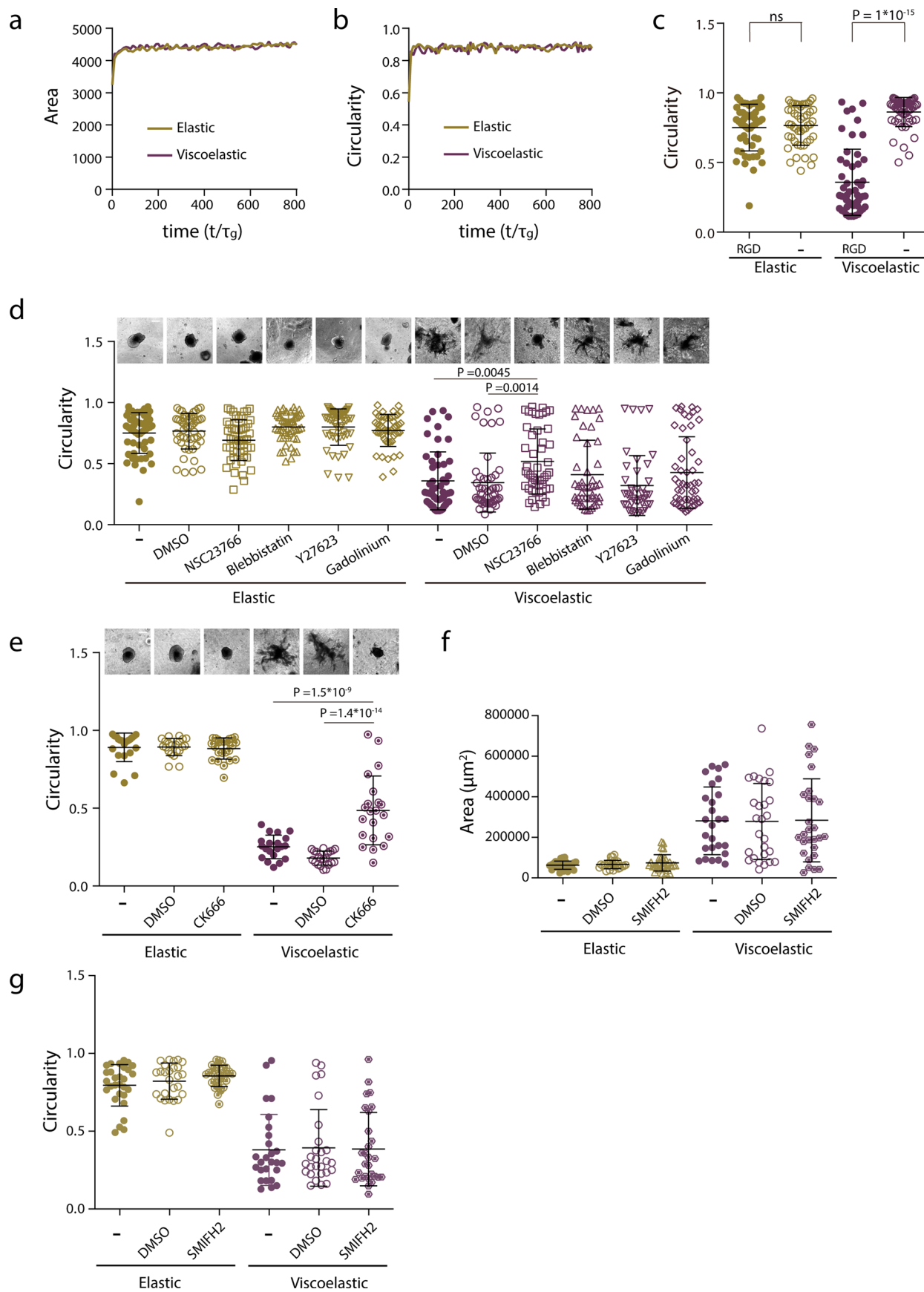
Extended Data Fig. 2 | Matrix viscoelasticity promotes epithelial to mesenchymal transition. **a-c**, quantification of mean fluorescence intensity of Snail, Slug and Zeb1 in spheroids in elastic and viscoelastic matrices. $n = 6$ gels per condition. **d, e**, quantification of percentage of Zeb2 positive cells (**d**) and mean Zeb2 fluorescence intensity (**e**) in spheroids in elastic and viscoelastic matrices. $n = 6$ gels per condition. **f**, quantification of mean fluorescence intensity of Slug cells in elastic and viscoelastic matrices encapsulated in vivo ($n = 9,10$ gels

per condition). **g**, quantification of number of Slug positive cells in spheroids in elastic and viscoelastic matrices encapsulated in vivo ($n = 9,10$ gels per condition). **h, i**, quantification of the area (**h**) and circularity (**i**) of MDA-MB-231 spheroids encapsulated in elastic and viscoelastic matrices. $n = 40$ spheroids per condition. Statistical analysis was performed using two-sided Mann-Whitney U-test. All data represent mean \pm s.d.



Extended Data Fig. 3 | 3D model for stress dependent cell flux simulations.
a, The texts in light blue/light red colour boxes describe the matrix/cell property and interactions therein. The yellow boxes represent the parameters which we vary to probe the phase space of morphologies. In this case the cell proliferation is stress dependent, hence cell flux is material property dependent. **b**, Volume of the tissue as a function of time for the elastic ($A = \frac{\tau_a}{\tau_m} = 0.4, \mu = \frac{\mu_t}{\mu_m} = 0.002$,

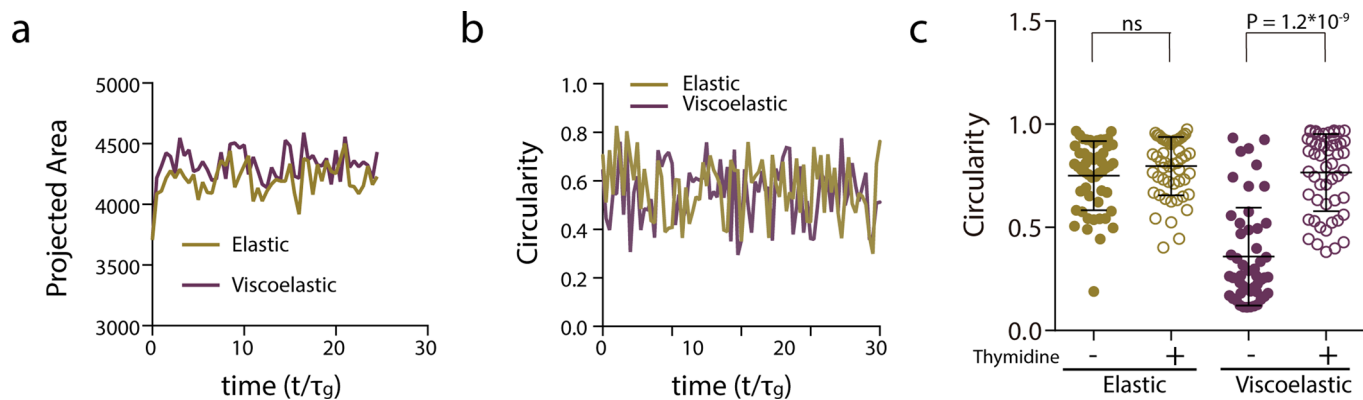
$j = \frac{\tau_g}{\tau_t} = 0.05$) and viscoelastic ($A = \frac{\tau_a}{\tau_m} = 400, \mu = \frac{\mu_t}{\mu_m} = 2, j = \frac{\tau_g}{\tau_t} = 0.22$) matrices (c) sphericity of the tissue as a function of time for elastic ($A = \frac{\tau_a}{\tau_m} = 0.4, \mu = \frac{\mu_t}{\mu_m} = 0.002, j = \frac{\tau_g}{\tau_t} = 0.05$) and viscoelastic ($A = \frac{\tau_a}{\tau_m} = 400, \mu = \frac{\mu_t}{\mu_m} = 2, j = \frac{\tau_g}{\tau_t} = 0.22$) matrices.



Extended Data Fig. 4 | See next page for caption.

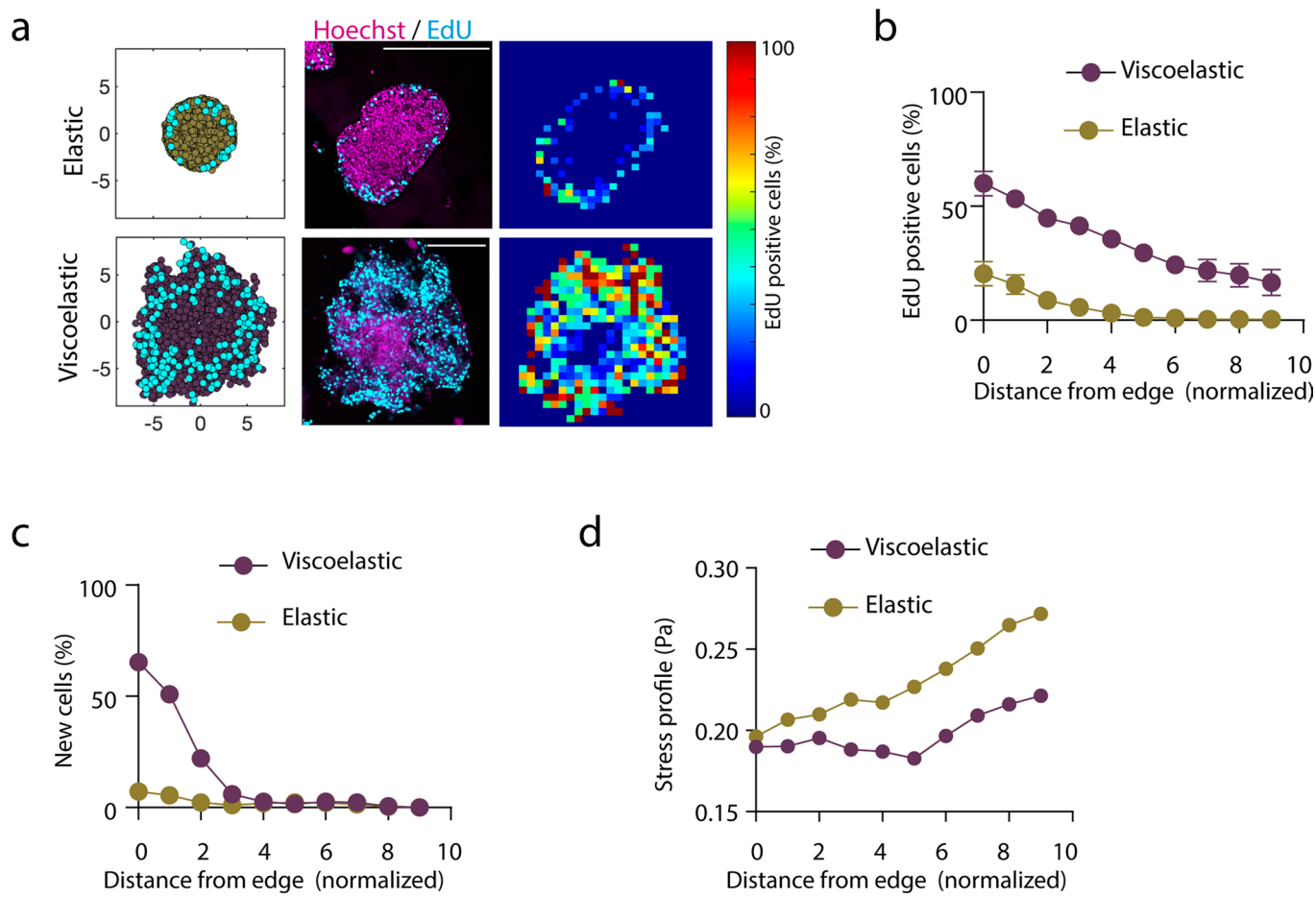
Extended Data Fig. 4 | Cell motility regulates tissue growth, symmetry breaking and fingering. **a, b**, Model prediction of spheroids projected area (**a**) and circularity (**b**) evolution with time when cell motility is suppressed, for stiff elastic ($A = \frac{\tau_a}{\tau_m} = 0.03$, $\mu = \frac{\mu_t}{\mu_m} = 0.002$, $j = \frac{\tau_g}{\tau_t} \sim 0$) and stiff viscoelastic ($A = \frac{\tau_a}{\tau_m} = 33.3$, $\mu = \frac{\mu_t}{\mu_m} = 2$, $j = \frac{\tau_g}{\tau_t} \sim 0$). **c**, Quantification of spheroids circularity after 5 days in hydrogels with and without cell adhesive ligand RGD. $n = 52, 52, 51, 54$ spheroids per condition. Statistical analysis was performed using Kruskal–Wallis test followed by post hoc Dunn’s test. **d**, Representative images (upper row) and quantification of spheroids circularity (lower row) after 5 days in hydrogels in the presence of the indicated inhibitors. $n = 52, 50, 51, 51, 51, 50, 51, 50, 51, 46, 41, 51$ spheroids per condition. Statistical

analysis was performed using Kruskal–Wallis test followed by post hoc Dunn’s test. **e**, Representative images (upper row) and quantification of spheroid’s circularity (lower row) after 5 days hydrogels in the presence of the indicated inhibitor. $n = 21, 21, 24, 20, 21, 25$ spheroids per condition. Statistical analysis was performed using Kruskal–Wallis test followed by post hoc Dunn’s test. **f, g**, Quantification of spheroids area (**f**) and circularity (**g**) of spheroids after 5 days in hydrogels in the presence of the indicated formins inhibitor. $n = 29, 26, 32, 26, 27, 28$ spheroids per condition. No significant differences were observed in the presence of the inhibitor. Statistical analysis was performed using Kruskal–Wallis test followed by post hoc Dunn’s test. All data represent mean \pm s.d.; all scale bars represent 200 μm .



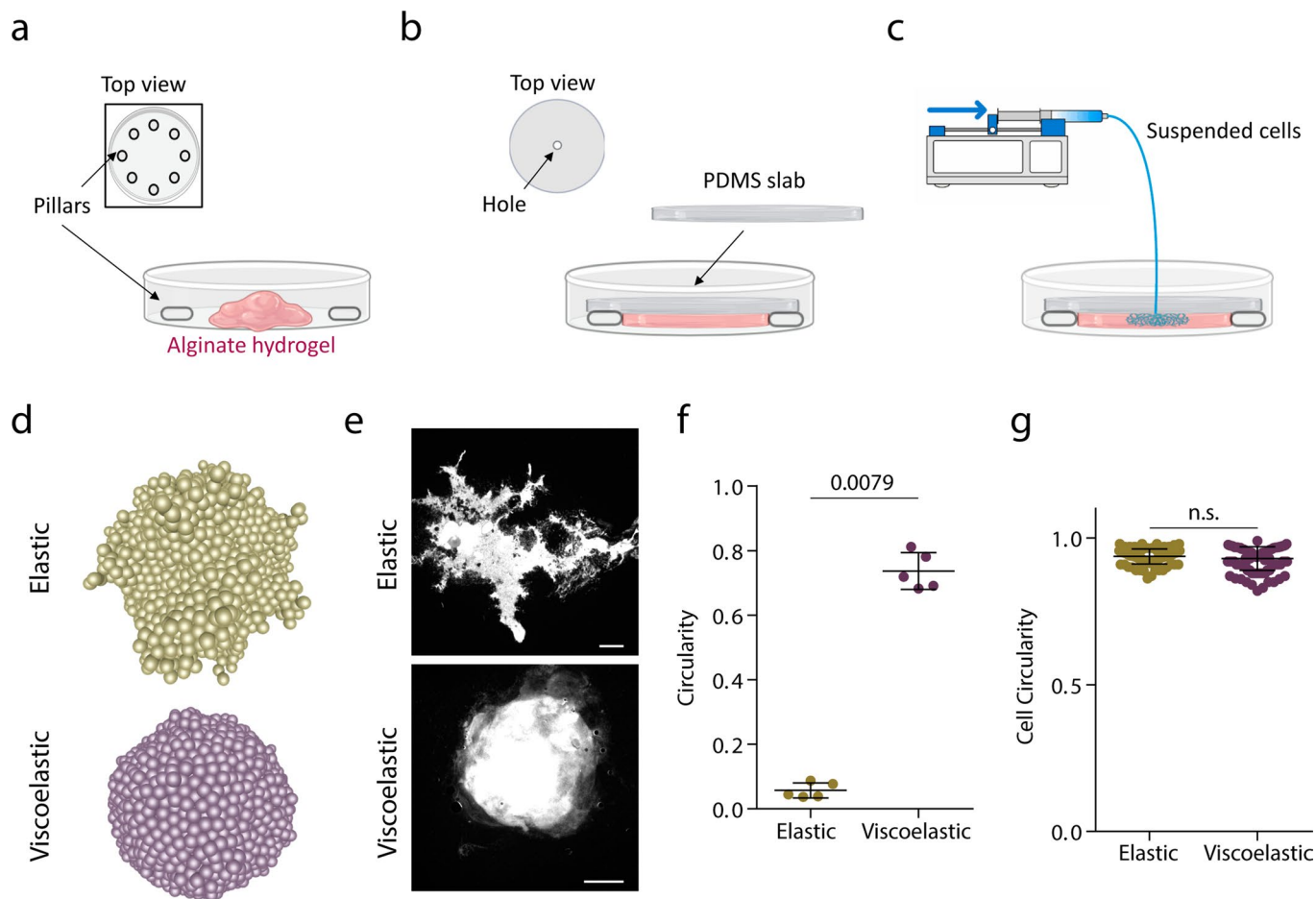
Extended Data Fig. 5 | Cell proliferation is required for tissue growth, symmetry breaking and fingering. a, b, Quantification from the simulations of the projected area (**a**) and circularity (**b**) of the spheroids, respectively, over time when proliferation is inhibited, for stiff elastic ($A = \frac{\tau_a}{\tau_m} = 0.4$, $\mu = \frac{\mu_t}{\mu_m} = 0.002$, $j = \frac{\tau_g}{\tau_t} = 0$) and stiff viscoelastic ($A = \frac{\tau_a}{\tau_m} = 400$, $\mu = \frac{\mu_t}{\mu_m} = 2$, $j = \frac{\tau_g}{\tau_t} = 0$)

matrices. **c**, Quantification of the circularity of spheroids without or in the presence of thymidine to inhibit cell proliferation. $n = 52, 53, 51, 53$ spheroids per condition. Statistical analysis was performed using Kruskal–Wallis test followed by post hoc Dunn’s test. All data represent mean \pm s.d.



Extended Data Fig. 6 | Cell proliferation is required for tissue growth, symmetry breaking and fingering. **a**, Simulation and Experimental results for the distribution of proliferating cells across spheroids in elastic (upper row) and viscoelastic gels (lower row): left, simulation example of the daughter cells (cyan) and the cells in the tissue spheroid (yellow elastic and cyan viscoelastic); centre, representative examples of experimental spheroids showing EdU-positive cells (cyan) and cell nuclei (Hoechst, magenta) for spheroids; right, colormaps showing the local percentage of Edu positive cells across the spheroid.

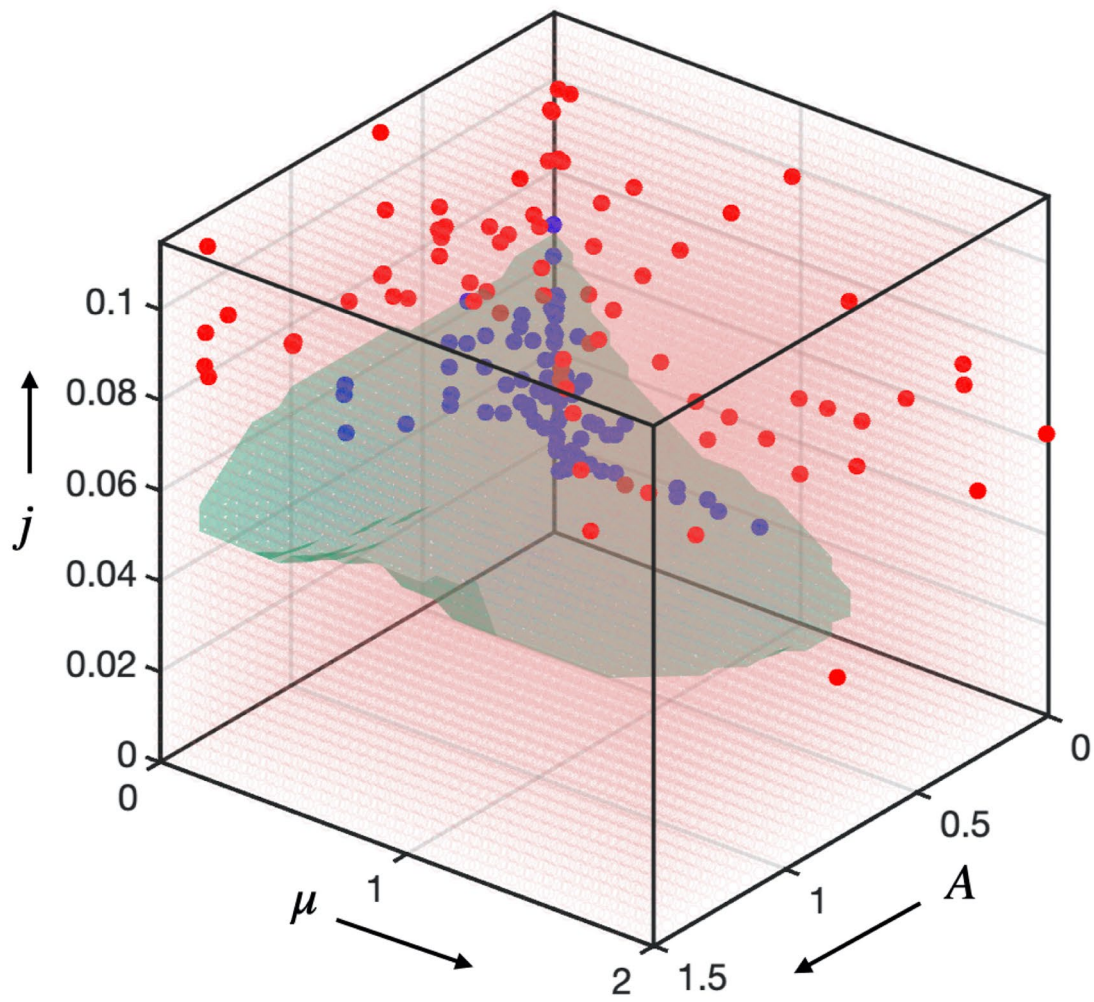
b-c, Experimental (**b**) and simulation results (**c**) showing the density proliferating cells depending of distance from the spheroid edge. $n = 3,4$ spheroids per condition. Error bars are s.e.m. All scale bars are $200 \mu\text{m}$. **d**, The normalized stress energy estimated from the simulations depending on the distance from the spheroid edge. The dimensionless parameter in the model for stiff elastic ($A = \frac{\tau_a}{\tau_m} = 0.4$, $\mu = \frac{\mu_t}{\mu_m} = 0.002$, $j = \frac{\tau_g}{\tau_t} = 0.05$) and stiff viscoelastic ($A = \frac{\tau_a}{\tau_m} = 400$, $\mu = \frac{\mu_t}{\mu_m} = 2$, $j = \frac{\tau_g}{\tau_t} = 0.22$) matrices.



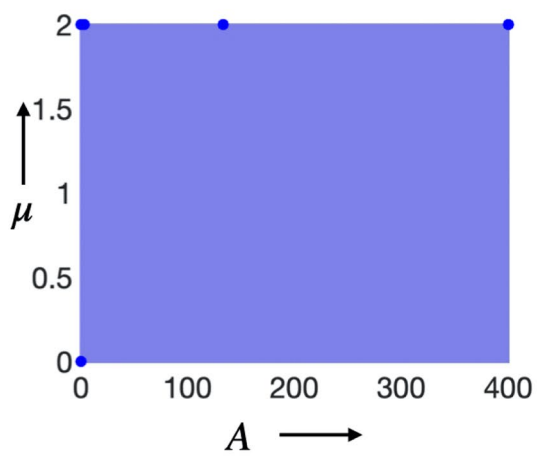
Extended Data Fig. 7 | Development of a microfluidic device to study the influence of pressure in tissue morphological stability. **a**, Pillars are distributed across the petri dish and an unpolymerized alginate solution is loaded. **b**, A PDMS slab is placed on top of the pillars and alginate is allowed to polymerize for 45 min. **c**, cells are loaded at a constant rate ($1 \mu\text{l}/\text{min}$) with a syringe pump through a hole in the PDMS slab. Due to the pressure ($\sim 19 \text{ kPa}$), cells displace the material. **d**, Model prediction for cell flux driven experiments for elastic ($A = \frac{\tau_a}{\tau_m} = 0.003, \mu = \frac{\mu_t}{\mu_m} = 0.002, j = \frac{\tau_g}{\tau_t} = 5$) and viscoelastic

($A = \frac{\tau_a}{\tau_m} = 3.33, \mu = \frac{\mu_t}{\mu_m} = 2, j = \frac{\tau_g}{\tau_t} = 5$) matrices. **e**, Examples of Hoechst staining of cells in elastic and viscoelastic matrices. Scale bar is $2000 \mu\text{m}$. **f**, Quantification of the circularity in elastic and viscoelastic hydrogels. $n = 5, 5$ experiments per condition. **g**, Quantification of single cells circularity inside tissues in elastic and viscoelastic hydrogels. $n = 100, 100$ cells per condition. Statistical analysis was performed using two-sided Mann-Whitney U-test. Data represent mean \pm s.d.

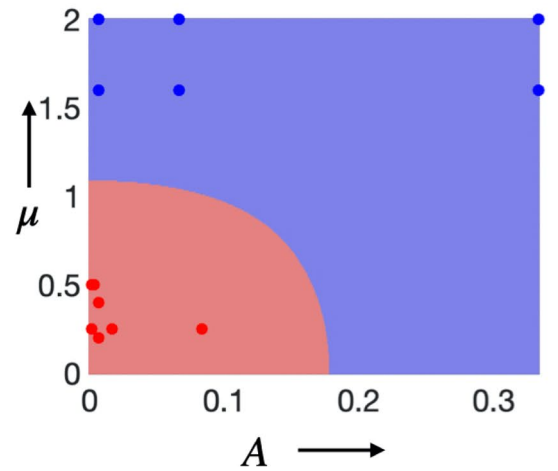
a



b



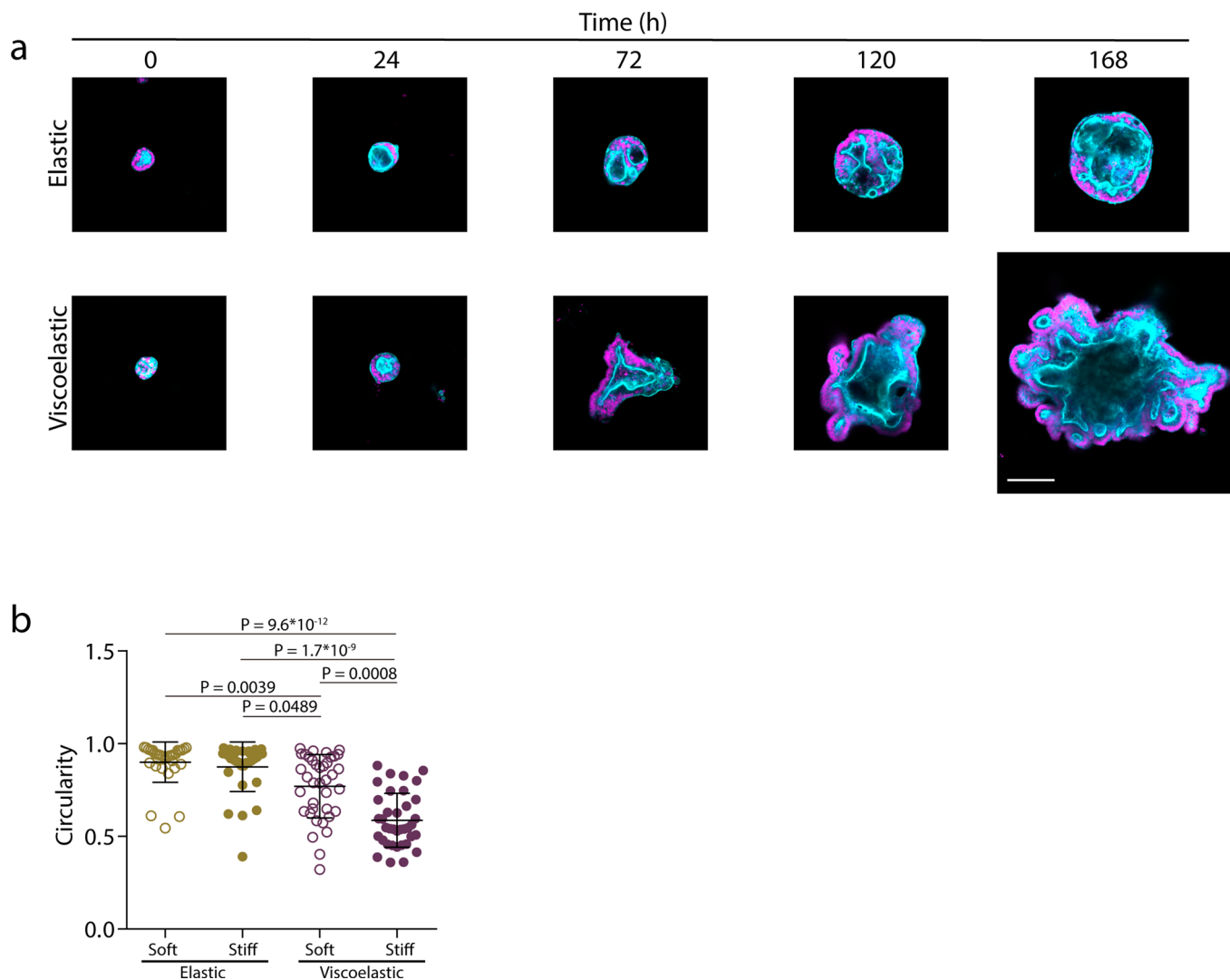
c



Extended Data Fig. 8 | See next page for caption.

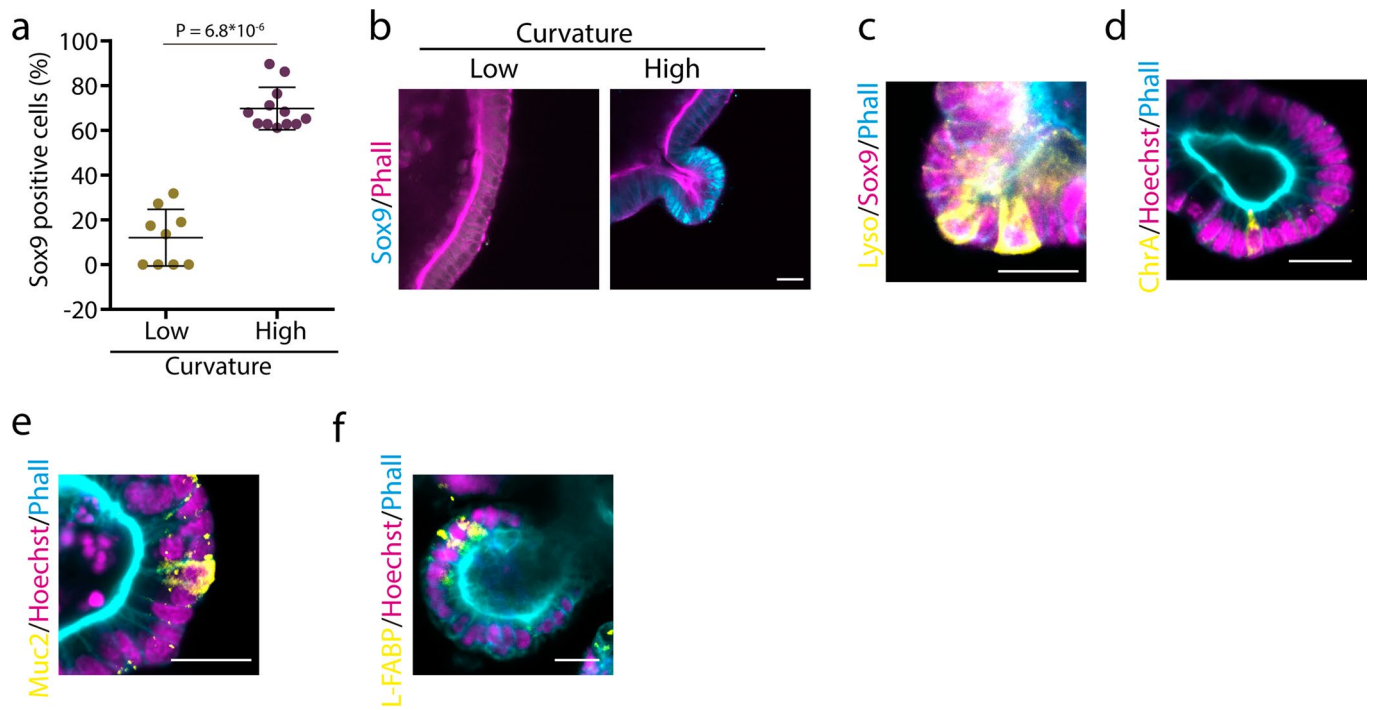
Extended Data Fig. 8 | Phase diagram simulations. **a**, 3D phase diagram including the results of multiple simulation runs utilized to determine the phase boundaries. Each dot represents the final result of a single simulation run under specific condition, and they are colour coded (blue = stable tissue growth; red = unstable tissue growth). **b**, A two-dimensional phase diagram for low motility case as a consequence of slow addition of cells, always leading to a stable spheroid (all blue). **c**, Two-dimensional phase diagram for the controlled cell-flux driven case where the addition of cells is fast. This leads to an inverted behaviour, the growth of tissue in elastic matrix (close to origin) is branched (red) and in viscoelastic matrix (away from origin) is a stable (blue). In **b** and **c**, the red and blue dots against represent data points extracted from individual simulations. When the scaled proliferation pressure $j = \frac{\tau_g}{\tau_t} \ll 1$, the tissue grows as a stable spheroid (Fig. 3i, j and Supplementary Figs. 7, 8). Additionally, when the scaled matrix relaxation time $A = \frac{\tau_a}{\tau_m} \ll 1$, the tissue remains spheroidal and is morphologically stable as long as the scaled proliferation pressure $j = \frac{\tau_g}{\tau_t} \sim O(1)$

(top panel of Figs. 1d, 3b, 4b). When the scaled matrix relaxation time $A = \frac{\tau_a}{\tau_m} \gg 1$: if the scaled proliferation pressure $j = \frac{\tau_g}{\tau_t} \ll 1$, the tissue grows as a stable spheroid (bottom right of Fig. 3i and bottom panel of Supplementary Fig. 8b); if the scaled proliferation pressure $j = \frac{\tau_g}{\tau_t} \sim O(1)$, the growth is unstable and the tissue breaks symmetry and develops fingers (bottom panel of Fig. 1d and bottom panel of Figs. 3b, 4b); if the scaled proliferation pressure $j = \frac{\tau_g}{\tau_t} \gg 1$, the morphological stability of the tissue depends on $\mu = \frac{\mu_t}{\mu_m}$ (see Extended Data Figs 7d, e, 8c); for $\mu = \frac{\mu_t}{\mu_m} \ll 1$, the tissue remains spheroidal (Extended Data Figs. 7d, e, 8c); for $\mu = \frac{\mu_t}{\mu_m} \gg 1$, growth is unstable and the tissue breaks symmetry and develops fingers (Extended Data Figs. 7d, e, 8c). viscoelastic limit are ($A = \frac{\tau_a}{\tau_m} = 0.017$, $\mu = \frac{\mu_t}{\mu_m} = 0.002$, $j = \frac{\tau_g}{\tau_t} = 0.05$) and ($A = \frac{\tau_a}{\tau_m} = 133$, $\mu = \frac{\mu_t}{\mu_m} = 2$, $j = \frac{\tau_g}{\tau_t} = 0.16$) respectively.



Extended Data Fig. 9 | Organoids grow, break symmetry and form buds with time. a, Examples of growth of intestinal organoids in elastic versus viscoelastic hydrogels over 7 days. Phalloidin in cyan, Hoechst in magenta. Scale bar is 100 μm . **b**, Quantification of organoid circularity in different stiffness elastic

and viscoelastic hydrogels. $n = 32, 32, 38, 37$ organoids per condition. Statistical analysis was performed using Kruskal–Wallis test followed by post hoc Dunn's test. Data represent mean \pm s.d.



Scales bar 20 μm

Extended Data Fig. 10 | Organoids present differentiated cell types.

a, Quantification of the percentage of Sox9 positive cells in low and high-curvature areas in organoids. $n = 9,12$ images per condition. Statistical analysis was performed using two-sided Mann-Whitney U-test. **b**, Representative examples. **c**, Organoid buds have lysozyme positive cells intercalated in between

Sox9 positive cells ($n = 15$ images). **d-f**, Organoids cultured in interpenetrating networks contain also **(d)** enteroendocrine ($n = 7$ images), **(e)** goblet cells ($n = 8$ images) and **(f)** enterocytes ($n = 5$ images). Data represent mean \pm s.d. Scale bars are 20 μm .